Supporting Information

Mixed-Valence Ru Nanoparticles Anchored on N-rich Metal–Phthalocyanine/Graphene vdW Heterostructures for Hydrogen-Bond-Assisted Alkaline Hydrogen Evolution

Zichong Xiang‡[a], Guanping Wei‡[a], Aifeng Yang[a], Shangyu Li[a], Sitian Xu[a], Yuelong Zhou[a], Longbin Li[a,b], Yiwang Chen*[a,b,c]*

Supplementary experimental section

Chemical Reagents and Materials.

N,N-Dimethylformamide (DMF 99.5%), sulfuric acid (H_2SO_4 98%), hydrochloric acid (HCl ≥ 98%), ethyl alcohol (C_2H_5OH 99.5%) were purchased from Xilong Technology Co., Ltd. Sodium hydroxide (NaOH ≥ 98%), potassium hydroxide (KOH 85%), Nafion (5 wt%), sodium sulfide nonahydrate ($Na_2S\cdot 9H_2O$), nickel (II) chloride ($NiCl_2$ 98%), ferrous chloride tetrahydrate ($FeCl_2\cdot 4H_2O$), and ammonium molybdate tetrahydrate ($(NH_4)_6Mo_7O_{24}\cdot 4H_2O$) were bought from Anhui Sensire Technology Co., Ltd. Ammonium hexachlororuthenate ($(NH_4)_2RuCl_6$) was obtained from Alab (Shanghai) Chemical Technology Co., Ltd. Graphene (SE1234-D) was bought from The Sixth Element (Changzhou) Materials Technology Co., Ltd. 20 wt% Pt/C was provided by innochemistry. 4-Nitrophthalimide ($C_8H_4N_2O_4$ 98%) was acquired from Saan Chemical Technology (Shanghai) Co., Ltd. Urea (CH_4N_2O) was provided by Shanghai Highnoon Biomedicine Technology Co., Ltd. Carbon paper was obtained from Hesen Electric Inc. Shanghai. All reagents were used without further purification.

Synthesis of the FeTNPc

0.994 g of $FeCl_2\cdot 4H_2O$, 3.84 g of 4-Nitrophthalimide, 10 g of urea and 50 mg of $(NH_4)_6Mo_7O_{24}\cdot 4H_2O$ was grind evenly in mortar. Then, the ground product was transferred to a round-bottom flask and heated at 180 °C for 6 hours under a nitrogen (N_2) atmosphere. After being allowed to cool naturally to ambient temperature, the product was sequentially washed once each with 1 M hydrochloric acid (HCl), 1 M sodium hydroxide (NaOH), and deionized water, followed by vacuum filtration after each washing step to remove impurities. The purified product was then subjected to lyophilization for 24 hours, yielding a dry and loose FeTNPc powder.

Synthesis of the NiTNPc and NiTAPc

The preparation of NiTNPc closely followed the procedure for FeTNPc, with the sole modification that $NiCl_2$ (anhydrous) was substituted for $FeCl_2 \cdot 4H_2O$ during reagent addition.

To convert NiTNPc into NiTAPc, a mixture of NiTNPc (0.3 g), $Na_2S \cdot 9H_2O$ (0.96 g), and DMF (6 mL) was combined in a round-bottom flask. The reaction mixture was heated at 60 °C for 1 hour under a nitrogen (N_2) atmosphere. Subsequently, the product was washed with deionized water and isolated by vacuum filtration, affording NiTAPc.

Synthesis of the NiFe PPc@G

For the preparation of 2D NiFe PPc, NiTAPc (0.3628 g), NiTNPc (0.215 g), FeTNPc (0.213 g), and KOH (0.327 g) were combined in 40 mL of DMF within a round-bottom flask. The mixture was heated at 150 °C for 24 hours under a nitrogen (N_2) atmosphere. After being allowed to cool naturally to ambient temperature, the product was washed three times with deionized water and subsequently dried under vacuum, yielding the intermediate product. Subsequently, the NiFe PPc intermediate and graphene were combined in a 1:3 mass ratio within a ball-milling jar. An appropriate amount of ethylene glycol was added as a process control agent to facilitate lubrication. Mechanical ball milling was performed at 1000 rpm for 2 hours. The resulting mixture was then collected, washed with deionized water, and isolated by vacuum filtration. Finally, the product was subjected to lyophilization, affording a loose 2D NiFe PPc material.

Synthesis of the Ru@NiFe PPc

Ru@NiFe PPc was fabricated via electrochemical deposition. The as-prepared 2D NiFe PPc material was first formulated into an ink. A corresponding volume of this ink solution was then drop-cast onto carbon paper (CP) with a target loading of 0.5 mg cm^{-2} and subsequently air-dried. Using the dried NiFe PPc/CP as the working electrode and a Pt foil as the counter electrode, electrochemical deposition was performed in an electrolyte solution containing 0.5 M H_2SO_4 and an appropriate amount of $(NH_4)_2RuCl_6$ dissolved in deionized water. Metallic Ru was deposited onto the NiFe PPc surface by conducting 375 cyclic voltammetry (CV) scans within the potential range of −0.6 to 0 V (vs. RHE) at a scan rate of 20 mV s^{-2}, resulting in the Ru@NiFe PPc composite.

Synthesis of the Ru@G

Ru@G was prepared using an electrochemical deposition procedure analogous to that employed for Ru@NiFe PPc, with the sole modification that the ink was replaced with a graphene dispersion. All other experimental conditions remained identical.

Materials characterization

Scanning electron microscope (SEM) images were obtained using a Zeiss Sigma 300. High-resolution transmission electron microscopy (HRTEM) images and energy-dispersive spectroscopy (EDS) elemental mapping were obtained using a Thermo Scientific Talos F200S G2 S/TEM. The aberration-corrected scanning transmission electron microscopy (AC-STEM) was performed using a JEOL ARM200F instrument. X-ray photoelectron spectroscopy (XPS) measurements were conducted using Thermo Fisher Scientific K-Alpha equipment to determine the valence states of cations in the pristine powder. Inductively Coupled Plasma Optical Emission Spectroscopy (ICP-OES) was performed using Agilent 720: apparatus to confirm the real chemical composition. The X-ray absorption fine structure (XAFS) measurements were conducted on Rapid XAFS HE Ultra (Anhui Absorption Spectroscopy Analysis Instrument Co., Ltd.) by transmission (or fluorescence) mode at 40 kV and 40 mA, and the Si (1860) spherically bent crystal analyzer with a radius of curvature of 500 mm was used for Ru. To confirm the crystalline structures, X-ray diffraction (XRD) was carried out in a Rigaku MiniFlex600 X-ray diffractometer (PXRD, 45 kV, 15 mA, Cu Kα radiation), and the data was refined in MID Jade 6 software. FTIR spectra were acquired using a Thermo Scientific™ Nicolet™ iS50 FTIR spectrometer, which operates across a broad spectral range of 15–27,000 cm^{-1}. UV-Vis spectra were measured with a Shimadzu UV2501PC spectrophotometer. The instrument covers a wavelength range of 190–1100 nm, with a testable range of 190–900 nm.

Electrochemical measurements.

All electrochemical measurements were carried out by CHI 760E electrochemical workstation

(Chenhua, Shanghai). A three-electrode system was established, comprising the prepared electrode, Pt sheet, and Hg/HgO electrode as the working electrode, counter electrode, and reference electrode To prepare catalyst ink, the 10 mg of electrocatalyst was evenly dispersed into 700 μL of deionized water, 200 μL of ethanol and 100 μL of 0.5 wt.% Nafion solution, and then 50 μL of ink was dropped onto the 1 x 1 cm^2 carbon paper with a loading amount of 0.5 mg cm^{-2}. Respectively, a 1.0 M KOH solution saturated with N_2 served as the electrolyte for performance evaluation. All applied potentials were converted to the reversible hydrogen electrode (RHE) scale using the formula $E_{RHE} = E_{Hg/HgO} + 0.059\times pH + 0.098$ V. Polarization curves were obtained via linear sweep voltammetry (LSV) measurement conducted at a scan rate of 5.0 mV s^{-1} without iR compensation. Electrochemical impedance spectroscopy (EIS) was performed to obtain Nyquist plots with a frequency range from 100 KHz to 0.01 Hz. Chronopotentiometry tests were conducted at a constant current density of 500 mA cm^{-2} for 90 h to assess long-term stability in 1 M KOH. The electrochemical active surface area (ECSA) was determined by measuring the capacitive current associated with double-layer charging from the scan-rate dependence of cyclic voltammetry (CV). Double-layer capacitances (C_{dl}) values were obtained at different scan rates (20, 40, 60, 80, and 100 mV s^{-1}) in a non-faradaic potential window. C_{dl} values of the samples were estimated by plotting the different in current density (Δj) between anodic and cathodic sweeps against the CV scan rate, with the slope of the resulting line equal to twice the C_{dl}. ECSA of the electrocatalyst was then calculated using the following formula:

$$\mathrm{ECSA} = \frac{C_{dl}}{C_s} \times \mathrm{Sgeometric}$$

where C_s is 40 μF cm^{-2} and $S_{geometric}$ is the geometric area of the electrode (1 cm^2).

Electrochemical measurements in AEM electrolyzer.

Alkaline water electrolyzer consist cathode and anode plates, cathode and anode catalysts, diaphragm, and Teflon gasketing. The leakage of electrolyte was avoided by Teflon gaskets. The Ru@NiFe PPc and commercial Pt/C (20 wt% Pt) were used as the cathodic catalysts, and benchmark NiFe layered double hydroxide was served as the anodic catalyst. AIKymer-75 was used as the anion exchange membrane (AEM). Prior to use, the membrane was cut into 2 cm × 2 cm pieces and pretreated by immersion in 1.0 M KOH solution for 24h at room temperature. Cathodic electrodes were fabricated by the catalyst coated membrane (CCM) method. Subsequently, the catalyst coated membrane was sandwiched with porous carbon paper (HCP120, Hesen) and Ni foam gas diffusion layers (GDLs) to assemble into a homemade integrated AEMWE device. Electrically insulating gaskets were also placed to prevent the liquid and gas from escaping through any space between flow fields. The alkaline water electrolyzer were connected to electrochemical analyzer. During operation, a peristaltic pump (Delxi) continuously circulated 1.0 M KOH electrolyte through both anode and cathode chambers at a flow rate of 90 mL min^{-1}. The operating temperature was maintained at 80°C in 1M KOH. Electrochemical measurements, including LSV and Dynamic Current Scanning Method, were carried out using a CS2350M electrochemical workstation (Creetest, Wuhan). The LSV measurements were performed at a scan rate of 5 mV s^{-1}. Long-term chronopotentiometry testing was evaluated under a constant current density of 500 mA cm^{-2}.

Computational details

All density functional theory (DFT) calculations were carried out using the Vienna ab initio Simulation package (VASP)[1] with the projector-augmented wave (PAW)[2] method. Spin-polarization was adopted for all of the calculations. The electron exchange interaction was described using the generalized gradient approximation (GGA) in the form of the Perdew−Burke-Ernzerhof (PBE) functional. The cut-off energy of plane-wave basis was set to 450 eV. The electronic and ionic convergence criteria were set to 1×10^{-5} eV and 0.02 eV/Å, respectively. The DFT-D3 method was employed to account for the effect of the long-range van der Waals (vdW) interactions.[3] Partial occupancies of the Kohn-Sham orbitals were enabled through Gaussian smearing with a width of 0.05 eV. The G-Ru_{13} model was constructed with a Ru_{13} nanocluster adsorbed onto a 6 × 6 graphene sheet. For the Ru@NiFe PPc system, the Ru_{13} nanocluster adsorbed onto the NiFe PPc/G heterojunction, which was constructed with VASPKIT package and exhibits a lattice mismatch below 0.3 %. A vacuum space of 15 Å was added to avoid the interactions between two periodic units. The k-space was sampled with a Gamma-centered grid of 3 × 3 × 1 in geometry optimizations and 5 × 5 × 1 in electronic properties calculations. To evaluate the catalytic activity of materials, the free energy change of each fundamental step was calculated using the computational hydrogen electrode (CHE) model with the equation $\Delta G = \Delta E + \Delta E_{ZPE} - T\Delta S + \Delta G_U + \Delta G_{PH}$. The ΔE, ΔE_{ZPE} and ΔS correspond to the electronic energies difference, zero-point energy change, and entropy change, respectively. The values of ΔE_{ZPE} and ΔS for adsorbates were obtained from vibrational frequency analysis. In this work, the temperature T was set to 298.15 K, and Bader charge population analysis was adopted to calculate the atomic charges.[3, 4]

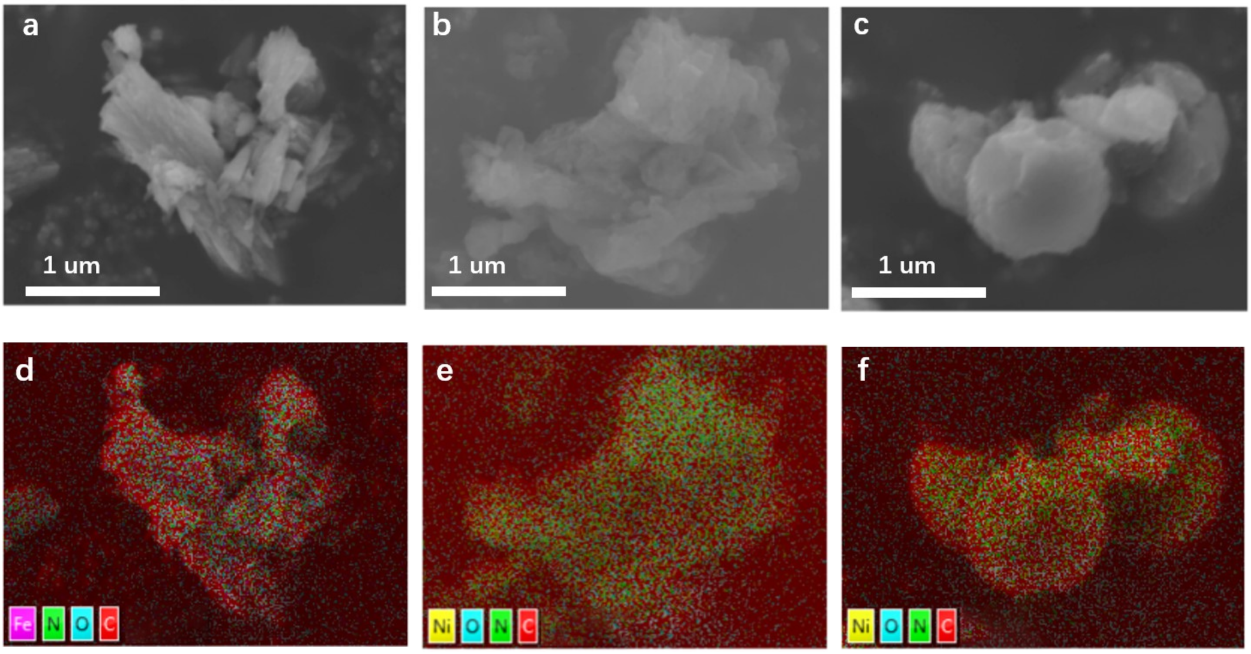

Fig. S1 SEM images of (a) FeTNPc, (b) NiTNPc, and (c) NiTAPc, the corresponding elemental mapping images of (d) FeTNPc, (e) NiTNPc, and (f) NiTAPc.

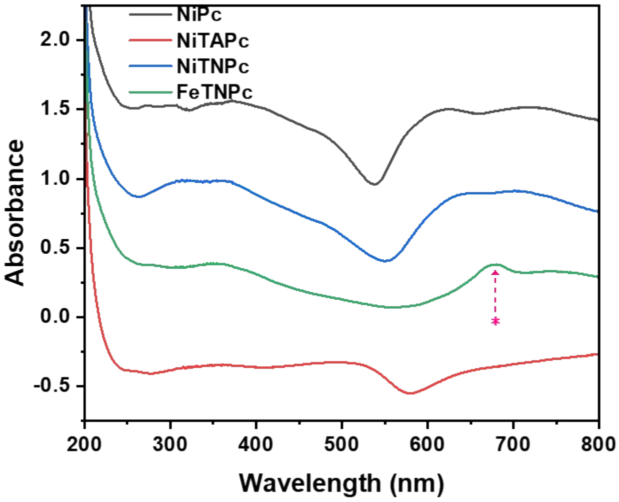

Fig. S2 UV-Vis absorption spectra of NiPc, NiTAPc, NiTNPc, and FeTNPc.

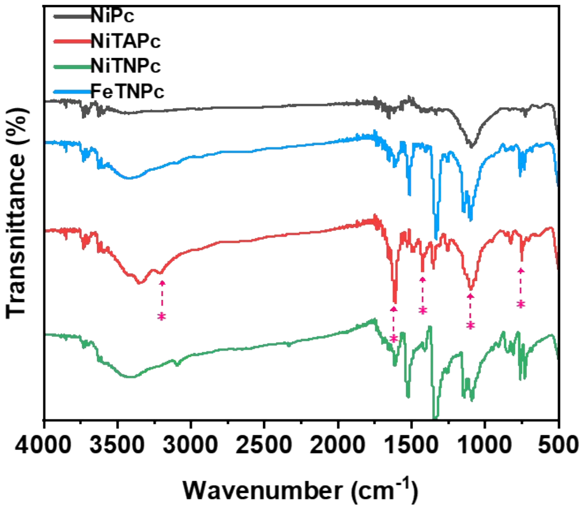

Fig. S3 FT-IR spectra of NiPc, NiTAPc, NiTNPc, and FeTNPc.

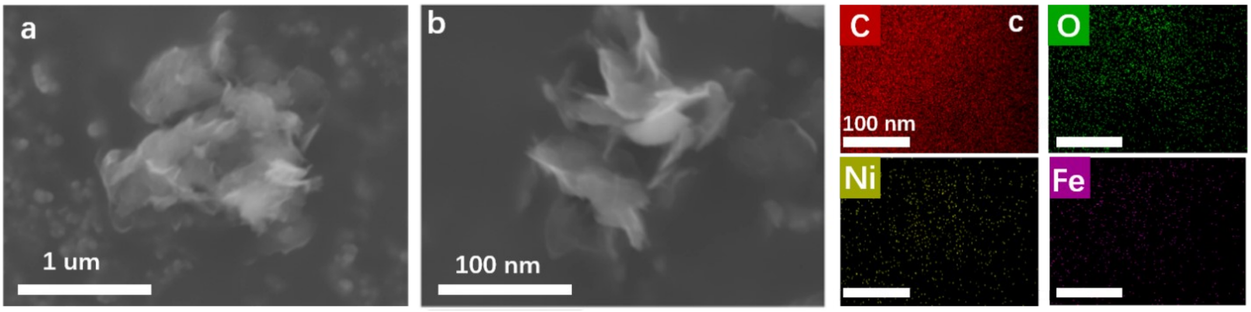

Fig. S4 SEM characterizations of NiFe PPc. (a), (b) SEM images at different magnifications. (c) Elemental mappings of C, O, Fe, Ni.

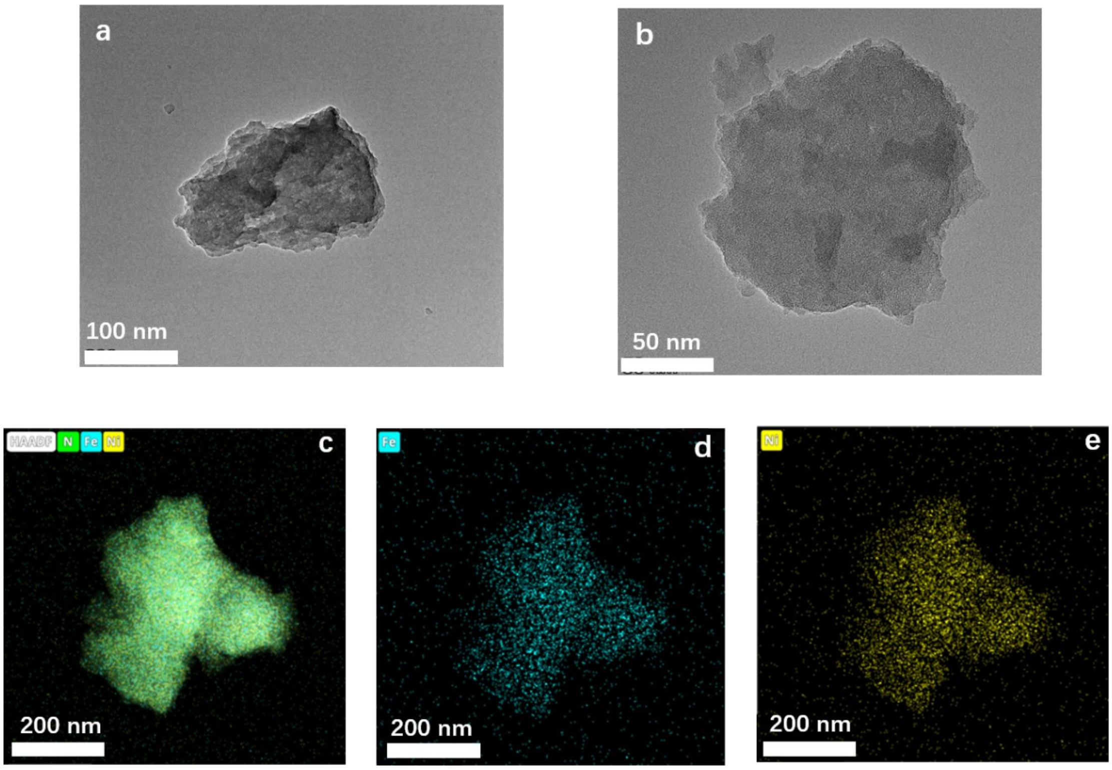

Fig. S5 TEM characterizations of NiFe PPc. (a), (b) TEM images at different magnifications. (c-e) Elemental mappings of N, Fe, Ni.

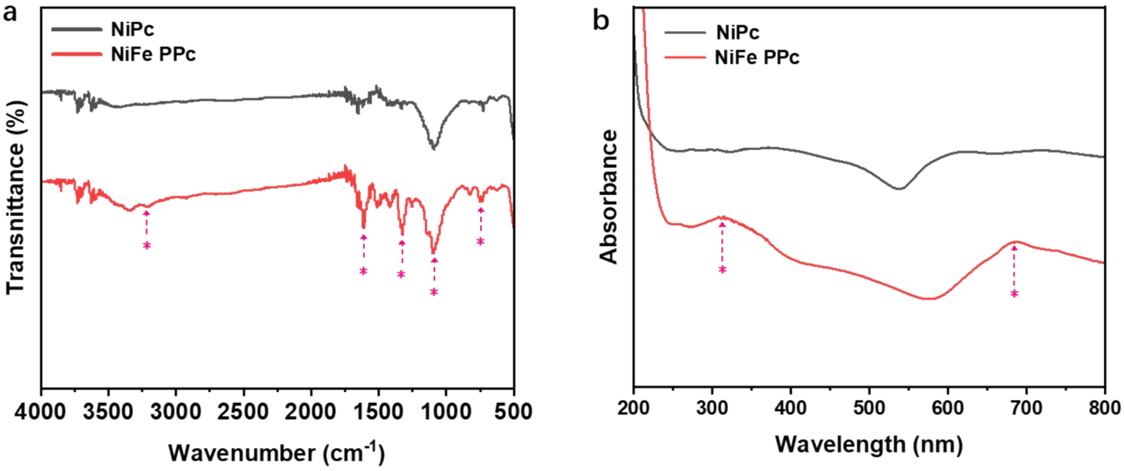

Fig. S6 (a) FT-IR spectra of NiPc and NiFe PPc. (b) UV-Vis absorption spectra of NiPc and NiFe PPc.

Note: The UV-Vis spectra of NiFe PPc showed two peaks ascribed to the characteristic peaks of Q-band (600-800 nm) and B-band (300-400 nm) of metal phthalocyanine structure, demonstrating the successful construction of the phthalocyanine macrocyclic structure.

In the infrared spectra, the peak at 3203 cm^{-1} corresponds to the N–H stretching vibration absorption band. The band at 1517 cm^{-1} is assigned to the antisymmetric stretching vibration of the nitro group on the aromatic ring, while the peak at 1606 cm^{-1}is attributed to the vibrational absorption of aromatic amines. The absorption bands at 1136 and 1902 cm^{-1} represent the characteristic absorption peaks of metal phthalocyanine, and the peaks at 843 and 817 cm^{-1} are associated with the typical absorption of trisubstituted benzene rings. Additionally, the bands at 729 and 760 cm^{-1}correspond to the fingerprint absorption region of phthalocyanine.

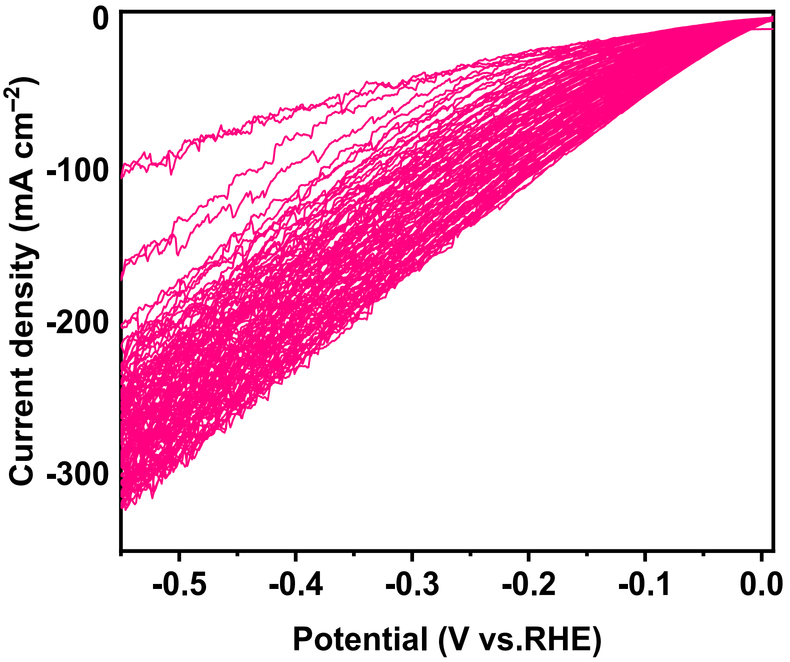

Fig. S7 The CV curves of Ru@NiFe PPc in 0.5 M H_2SO_4 $(NH_4)_2RuCl_6$ at 20 mV s^{-1}.

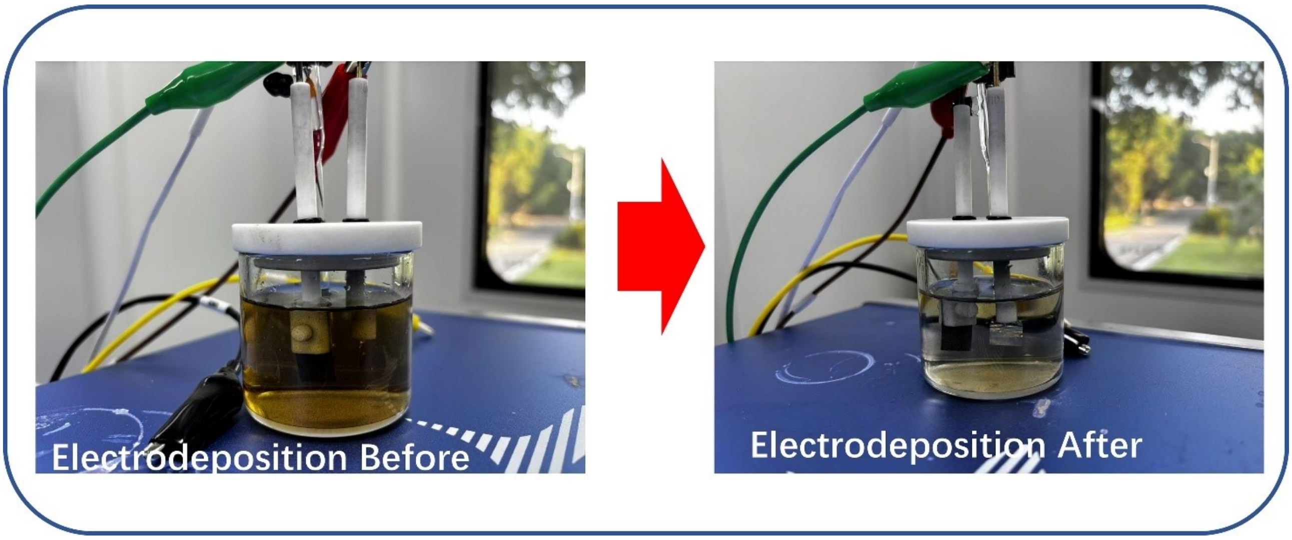

Fig. S8 The optical photographs of deposition solution before and after electrochemical deposition process.

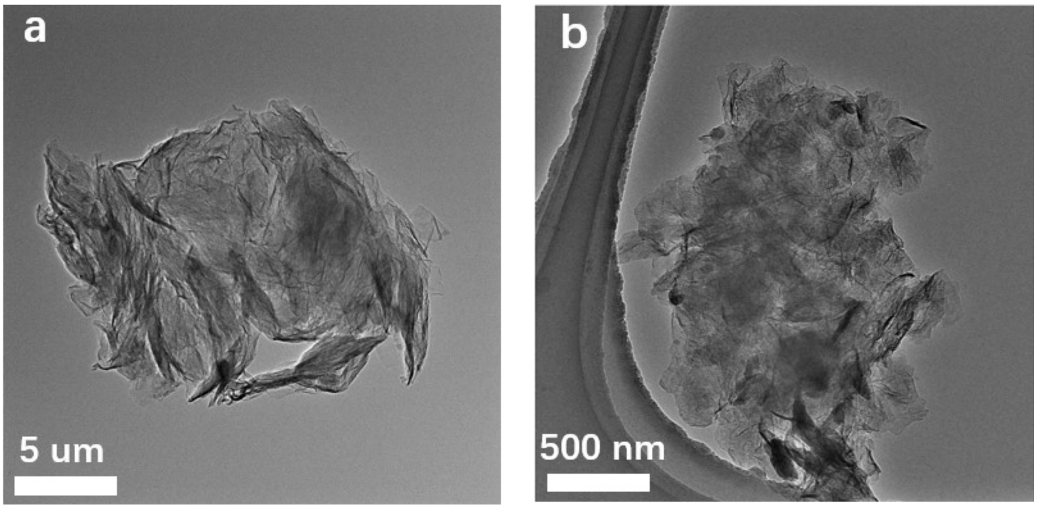

Fig. S9 TEM images of Ru@NiFe PPc at different magnifications. (a) low magnification and (b) high magnification.

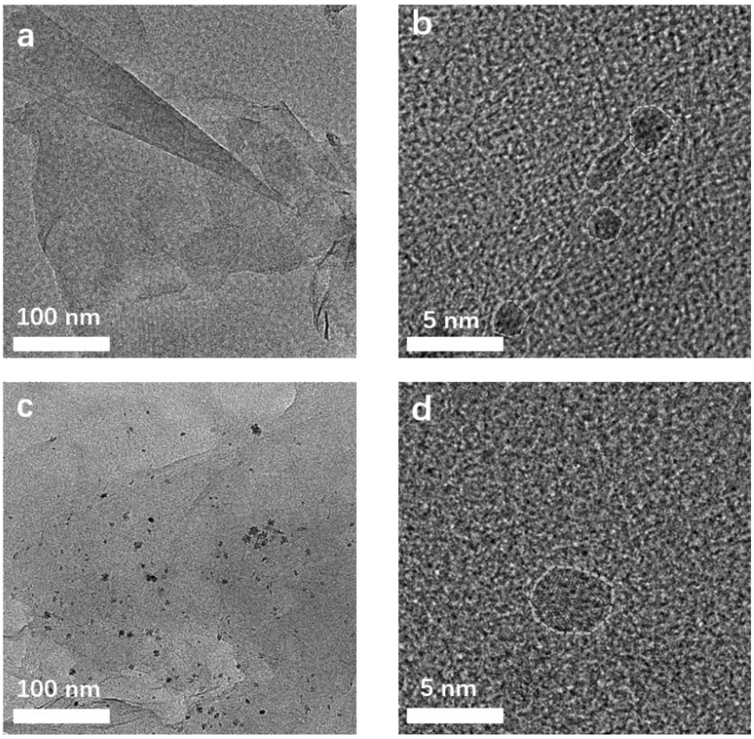

Fig. S10 TEM images at different magnifications. (a), (b) Ru@NiFe PPc, (c), (d) Ru@G.

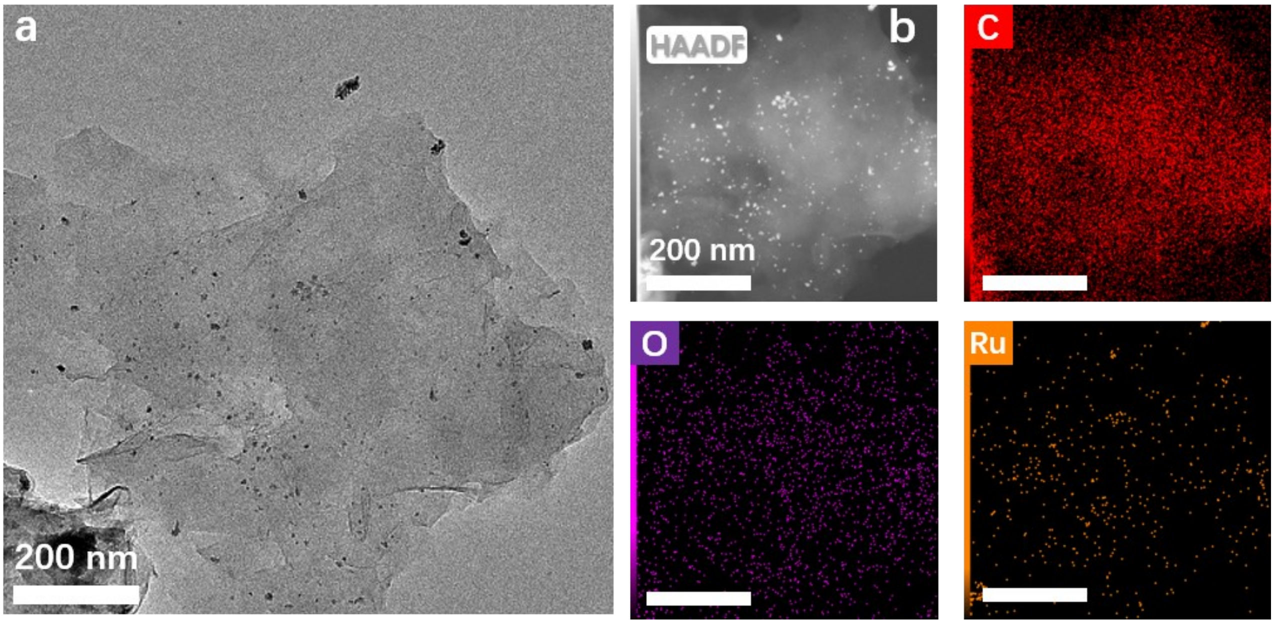

Fig. S11 TEM characterizations of Ru@G. (a) TEM image, (b) HAADF-TEM and corresponding EDX elemental mapping images.

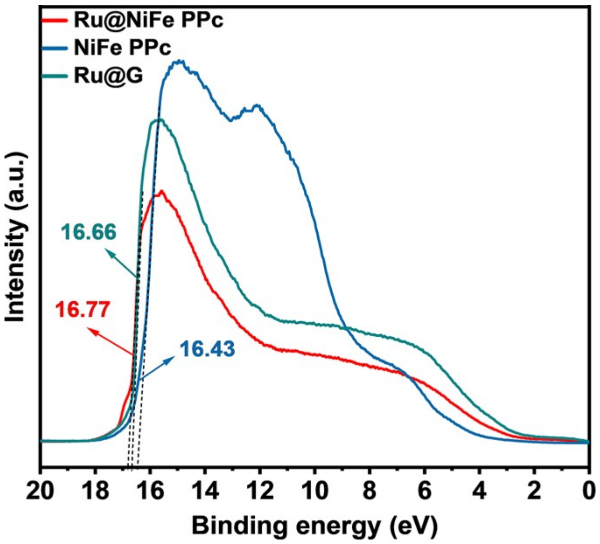

Fig. S12 UPS spectra of Ru@NiFe PPc, NiFe PPc, and Ru@G.

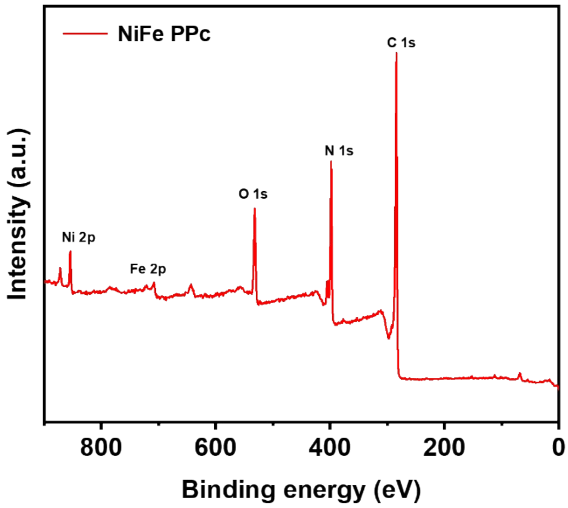

Fig. S13 XPS survey spectrum of the NiFe PPc.

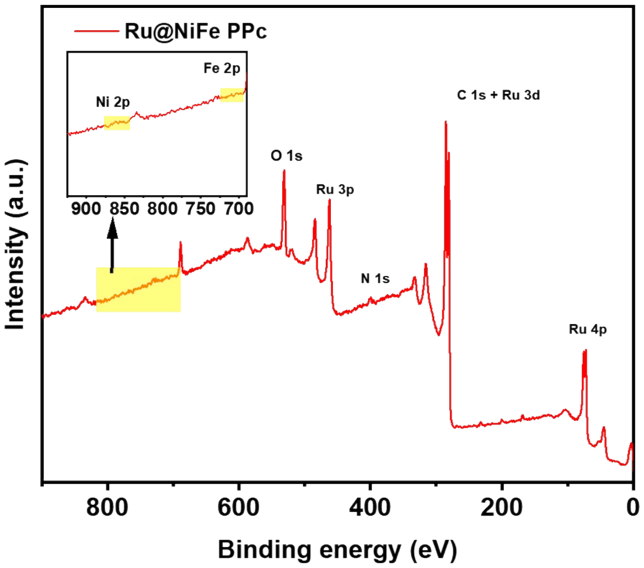

Fig. S14 XPS survey spectrum of the Ru@NiFe PPc.

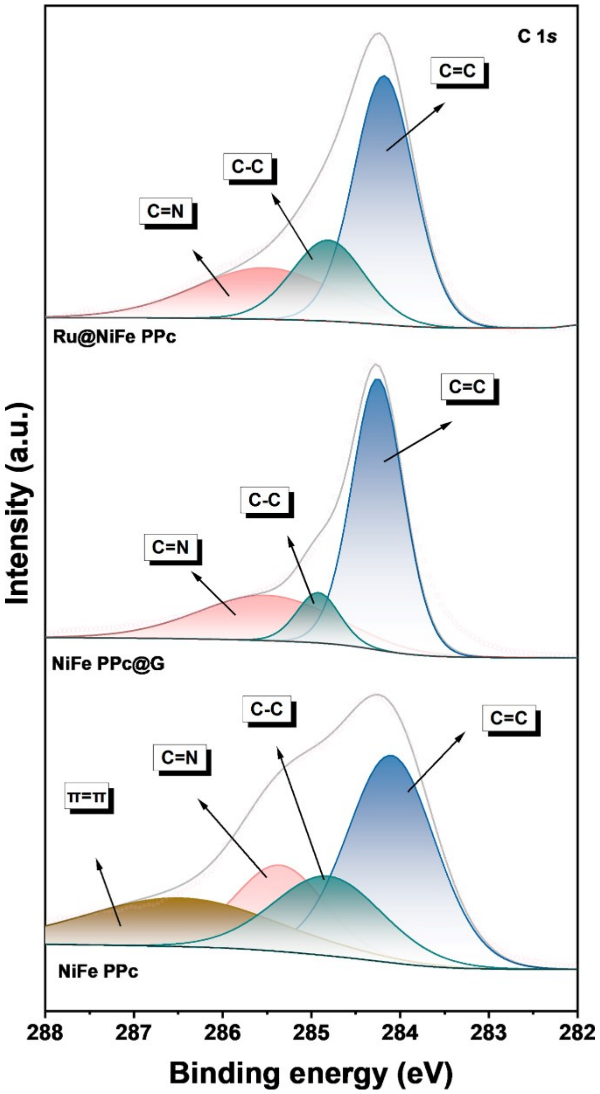

Fig. S15 HR-XPS spectra of C1s of the Ru@NiFe PPc, NiFe PPc and NiFe PPc@G.

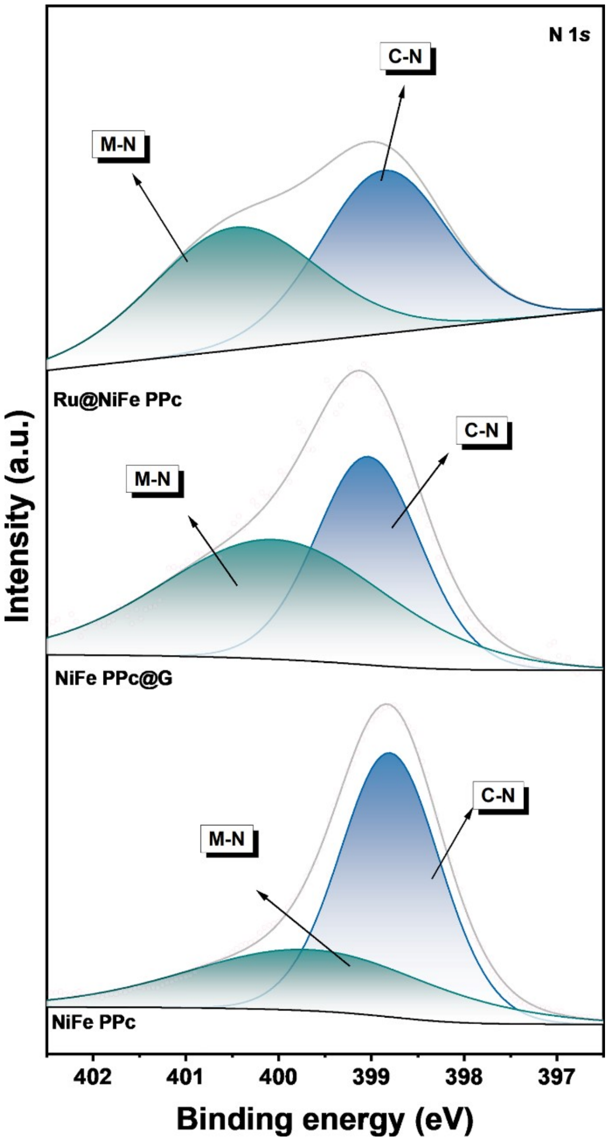

Fig. S16 HR-XPS spectra of N1s of the Ru@NiFe PPc, NiFe PPc and NiFe PPc@G.

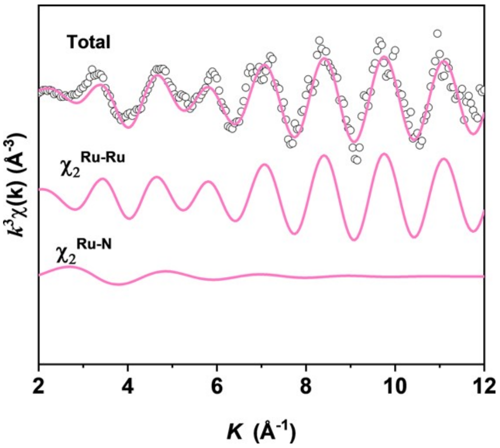

Fig. S17 The EXAFS analysis of 3D-G-PFePc in k space.

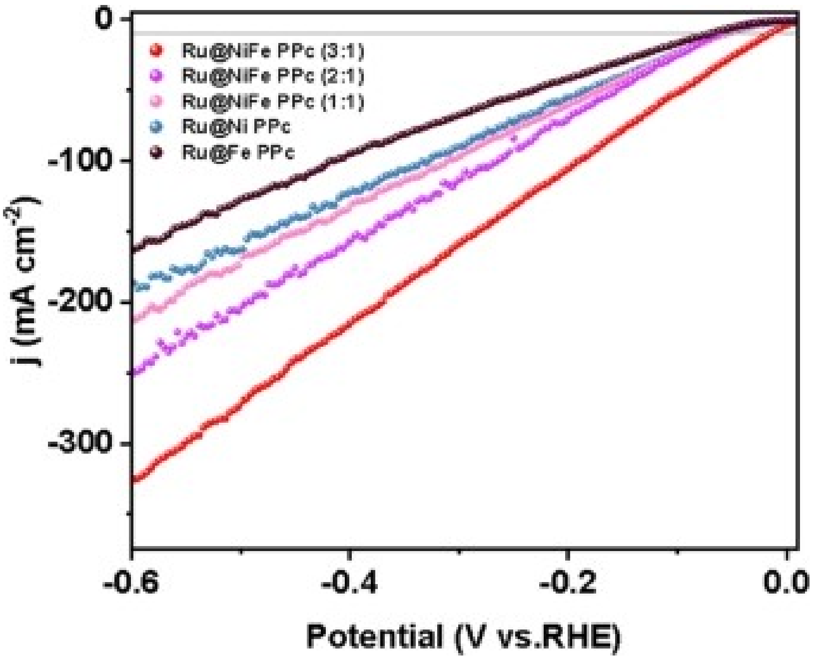

Fig. S18 Comparison of LSV curves at different Ni/Fe phthalocyanine ratios.

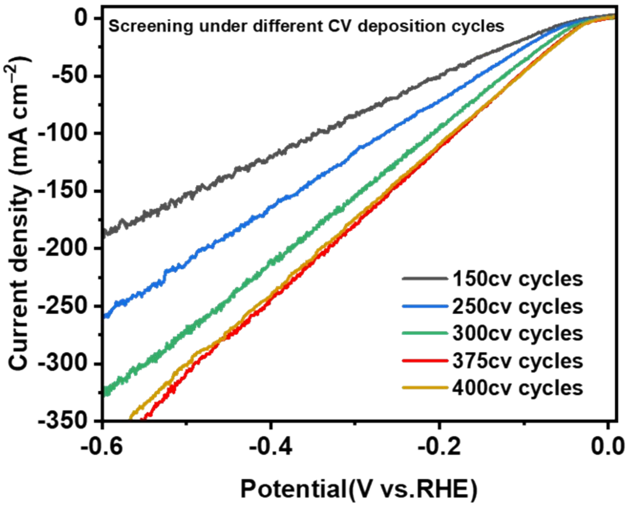

Fig. S19 LSV curves of Ru@NiFe PPc samples electrochemically deposited with different numbers of CV cycles (150–400 cycles).

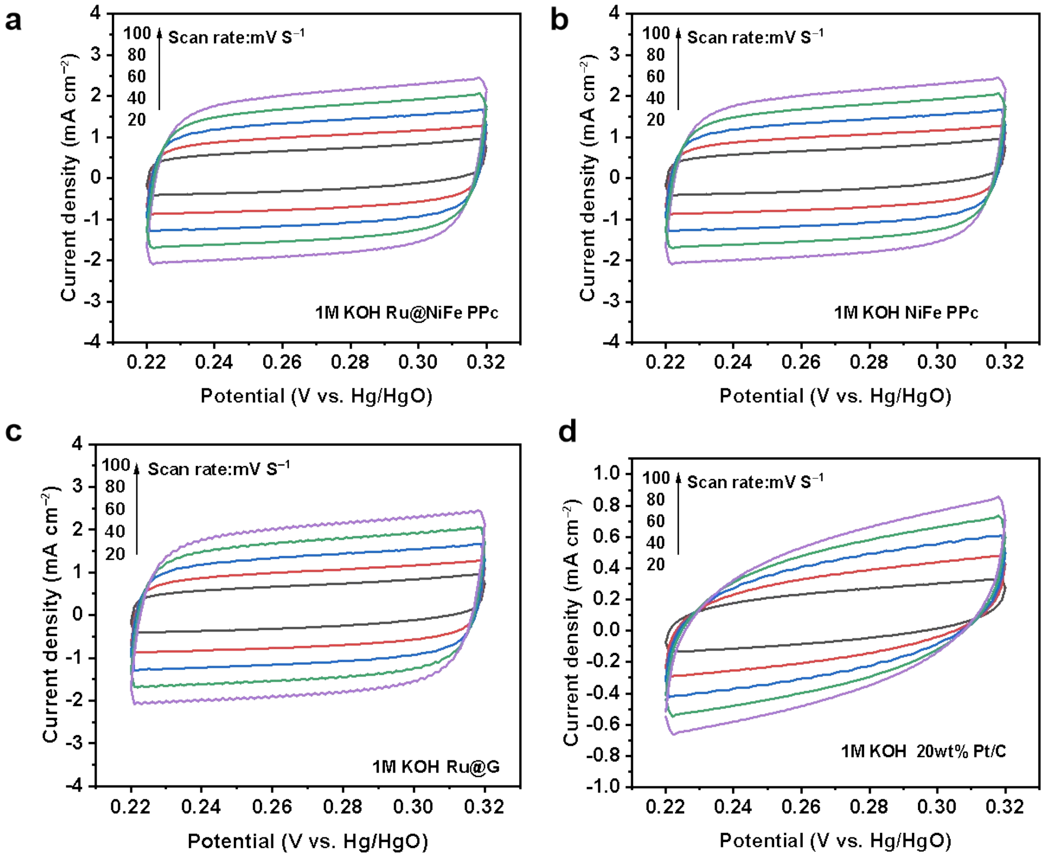

Fig. S20 CV curves of the (a) Ru@NiFe PPc, (b) NiFe PPc, (c) Ru@G, and (d) 20 wt% Pt/C, electrocatalysts with varying scan rates from 20 to 100 mV s^{-1}.

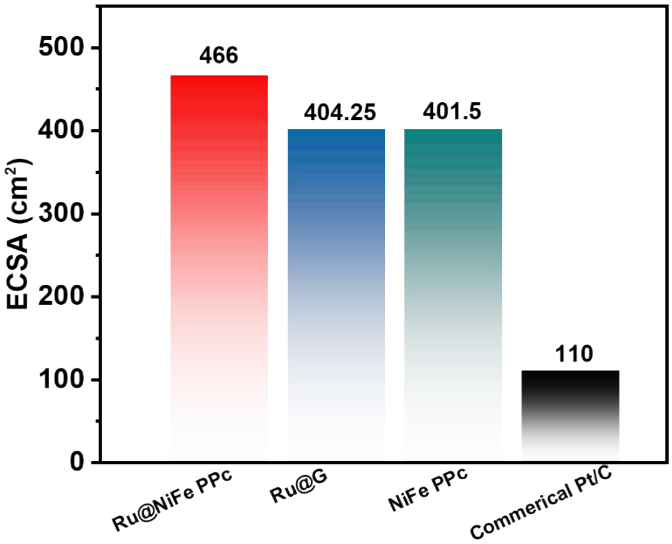

Fig. S21 Comparison of ECSAs for Ru@NiFe PPc, Ru@G, NiFe PPc, and Commerical Pt/C in this work.

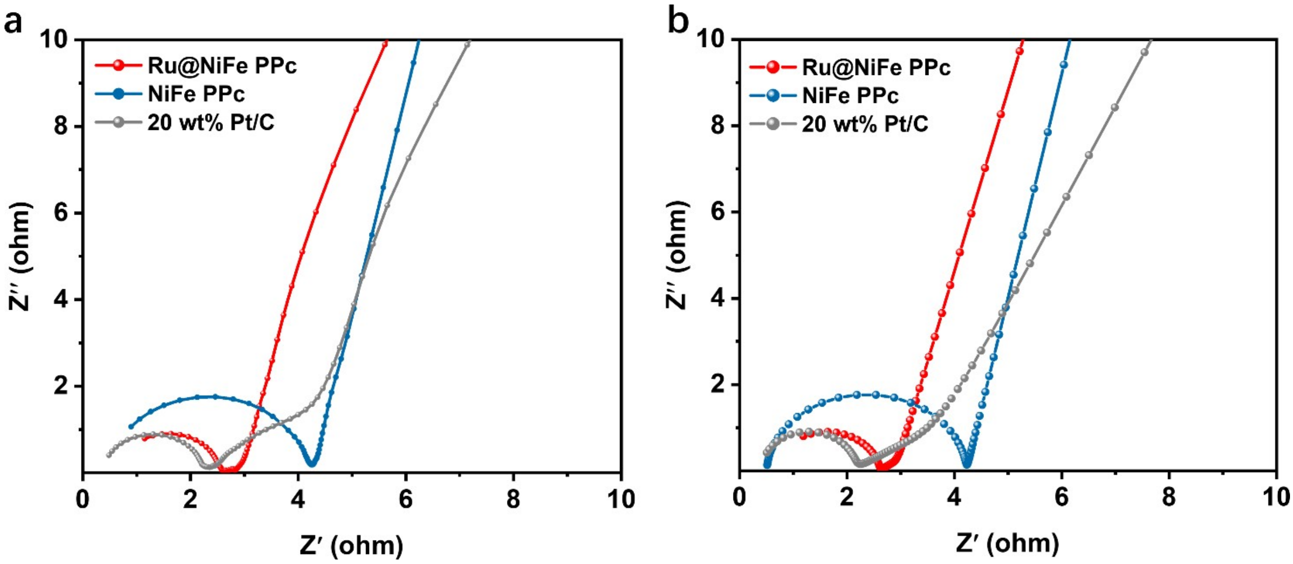

Fig. S22 Nyquist plots of Ru@NiFe PPc, NiFe PPc, and 20 wt% Pt/C in 1 M KOH. (a) Experimental Nyquist plots. (b) The fitting Nyquist plots.

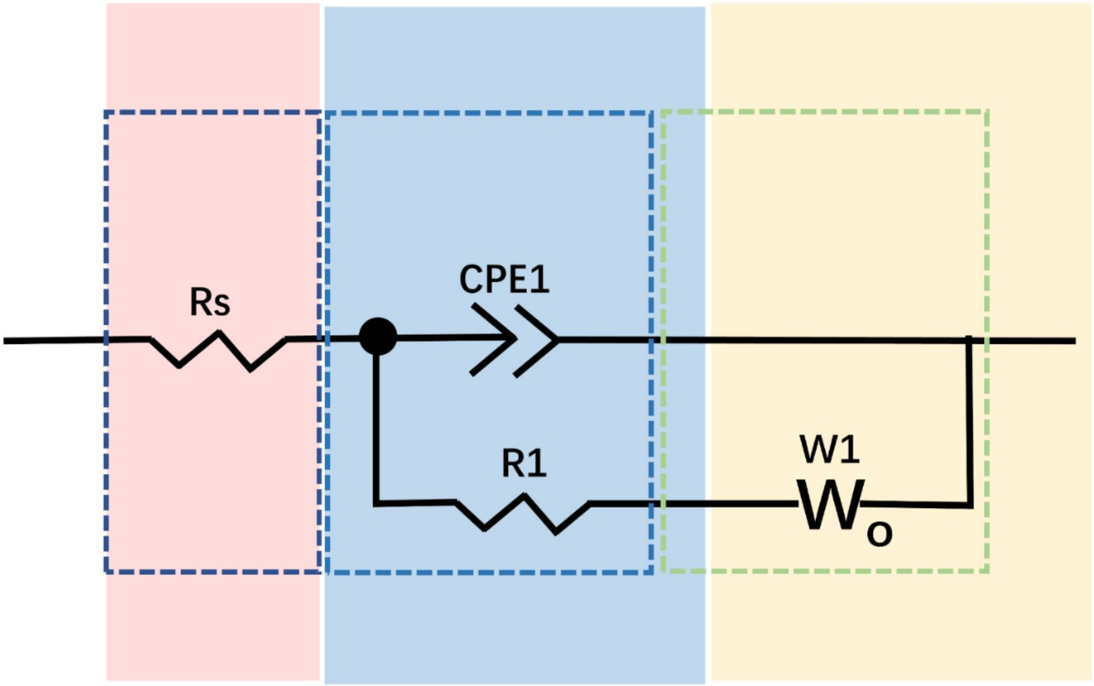

Fig. S23 The equivalent circuits for HER of Ru@NiFe PPc in 1 M KOH.

Note: The applied equivalent circuit consists of a solution resistance (**Rs**) in series with a parallel combination of a charge-transfer resistance (**R1**) and a constant phase element (**CPE1**), followed by diffusion element (**W1**). **Rs** represents the uncompensated electrolyte resistance. The parallel branch of **R1** and **CPE1** describes the interfacial charge-transfer process associated with hydrogen adsorption/desorption and the non-ideal double-layer capacitance originating from surface heterogeneity. The element **W1** accounts for the ion or intermediate diffusion behavior at low frequencies, reflecting the mass-transport limitations near the electrode/electrolyte interface.

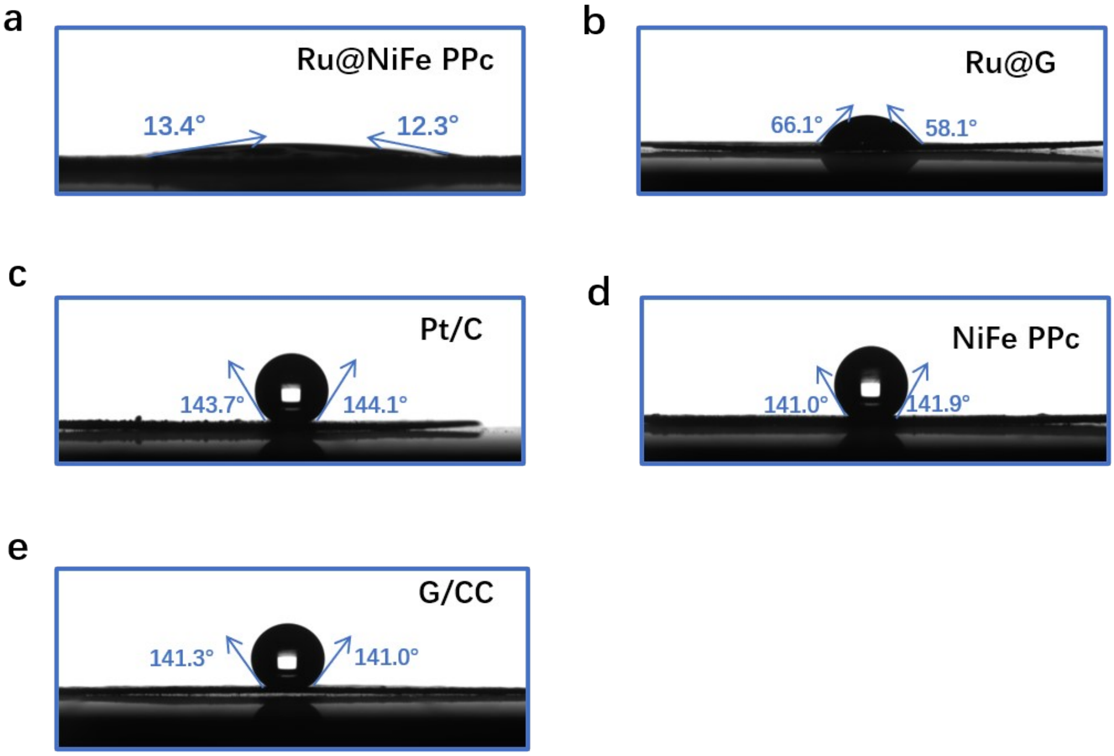

Fig. S24 Optical image of water contact angle of the (a) Ru@NiFe PPc, (b) Ru@G, (c) 20 wt% Pt/C, (d) NiFe PPc, and (e) G/CC.

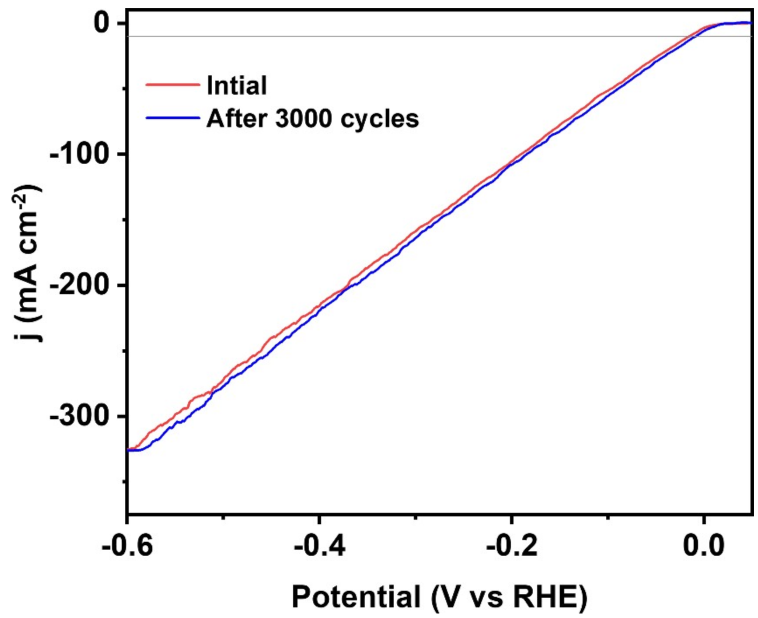

Fig. S25 Polarization curves of Ru@NiFe PPc before and after 3000 cyclic voltammetry tests.

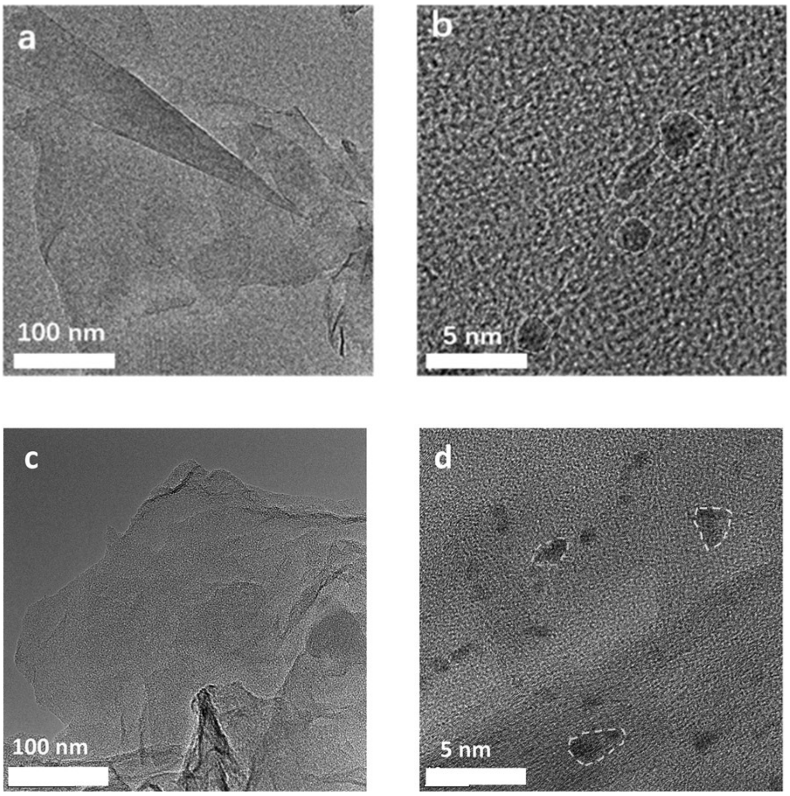

Fig. S26 TEM images at different magnifications. (a), (b) Ru@NiFe PPc, (c), (d) Ru@NiFe PPc after 3000 CV cycles.

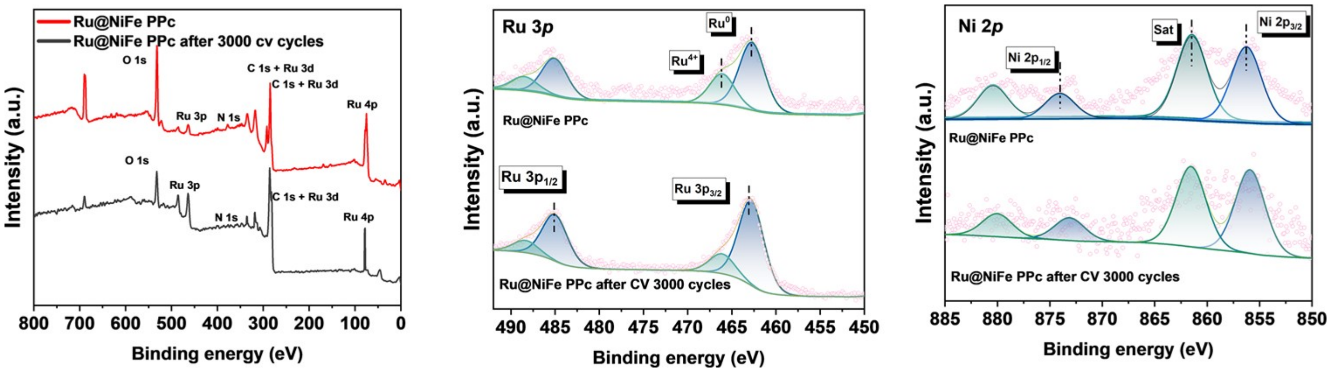

Fig. S27 (a) XPS survey spectra of the Ru@NiFe PPc and Ru@NiFe PPc after 3000CV cycles. (b) HR-XPS spectra of Ru 3p. (c) HR-XPS spectra of Ni 2p.

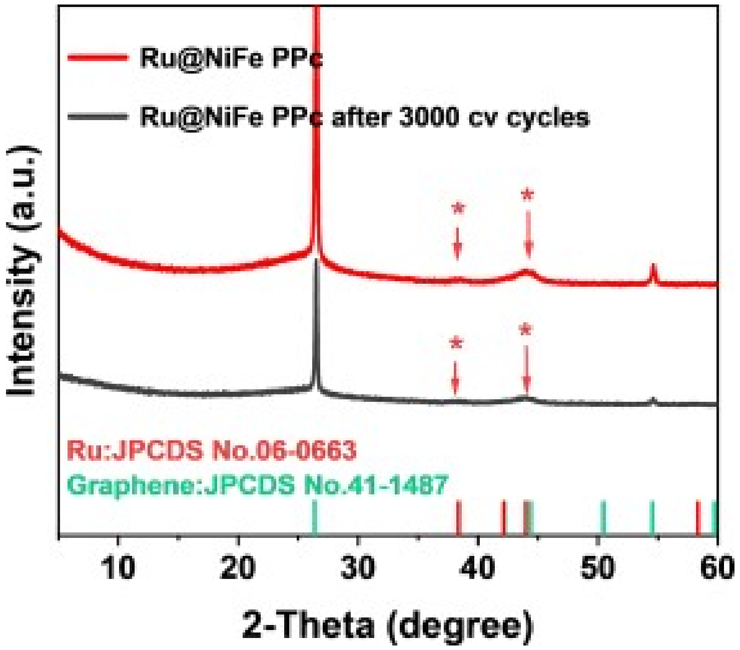

Fig. S28 XRD patterns of the Ru@NiFe PPc and Ru@NiFe PPc after 3000 CV cycles.

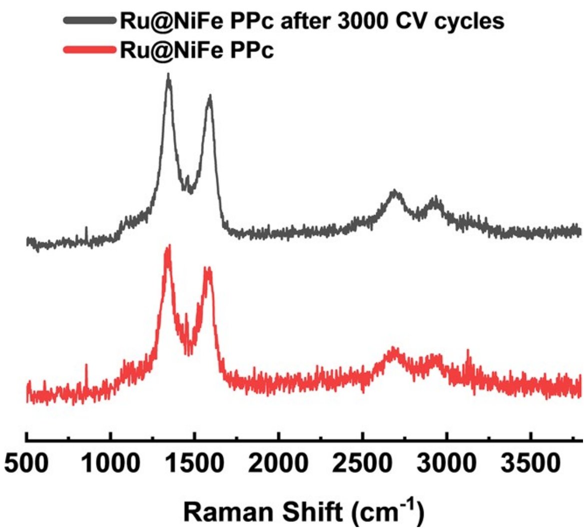

Fig. S29 Raman spectra of Ru@NiFe PPc and Ru@NiFe PPc after 3000 CV cycles.

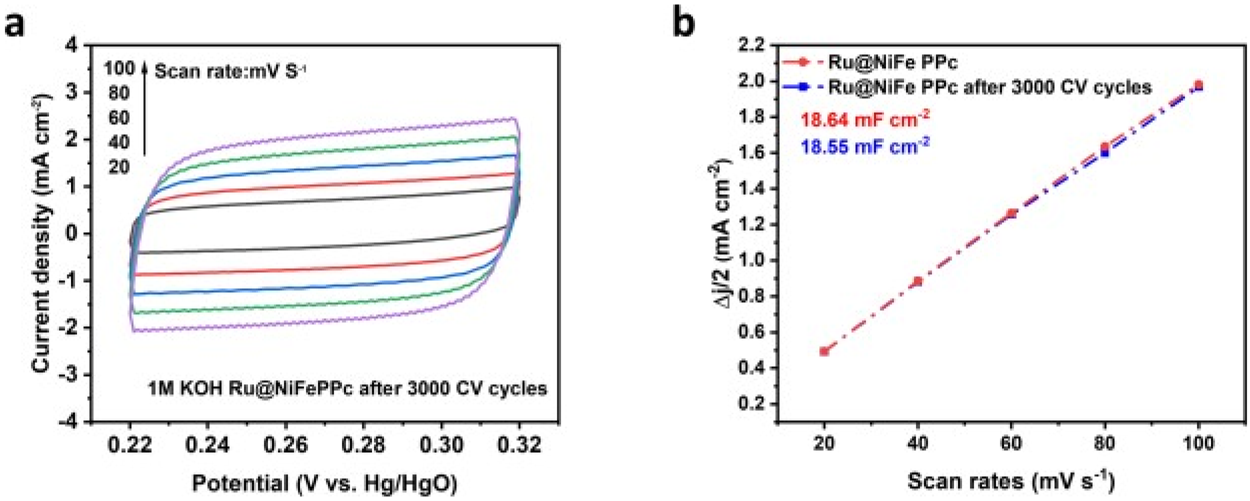

Fig. S30 (a) CV curves of the Ru@NiFe PPc after 3000 CV cycles. (b) Corresponding estimation of C_{dl} by plotting the current density variation.

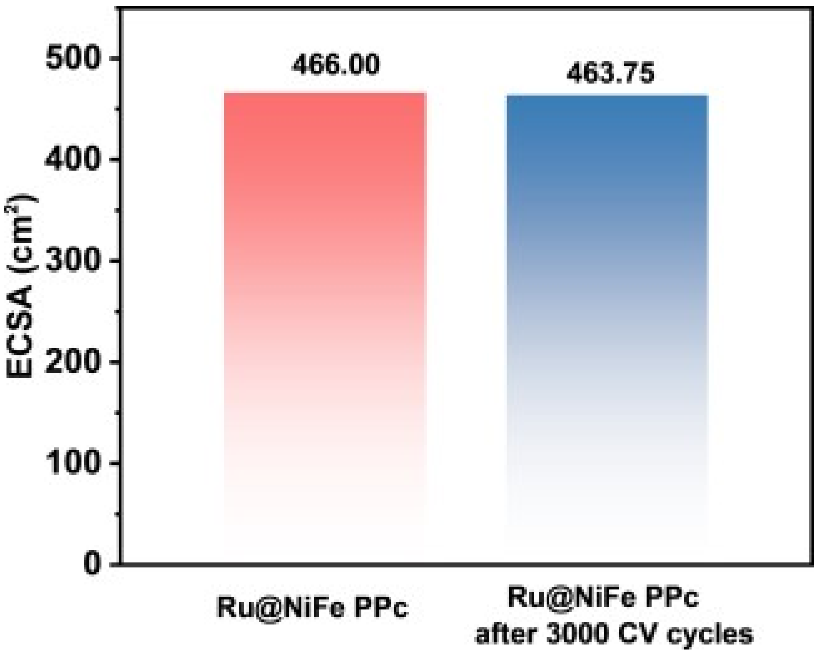

Fig. S31 Comparison of ECSAs for Ru@NiFe PPc, Ru@G and Ru@NiFe PPc after 3000 CV cycles in this work.

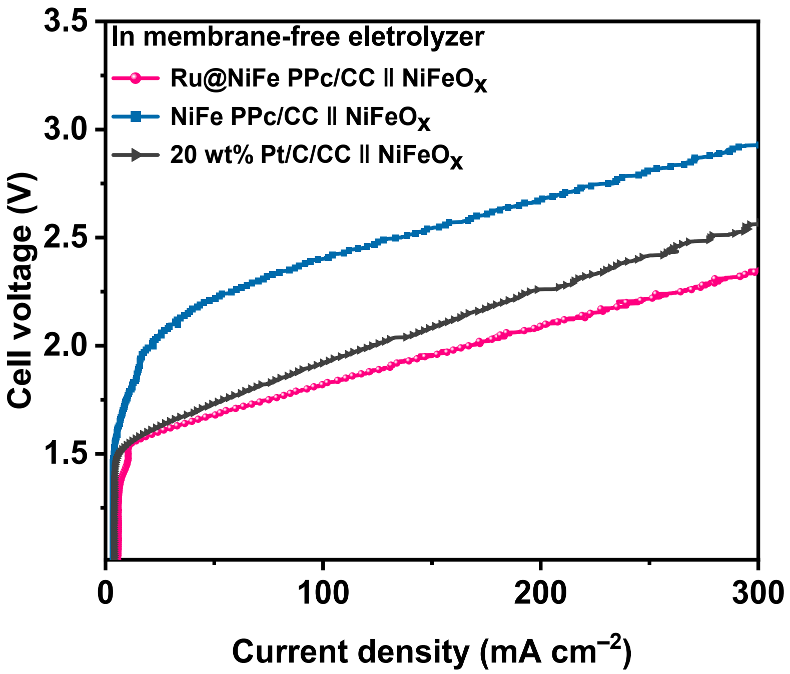

Fig. S32 Polarization curves of overall water splitting for Ru@NiFe PPc (-) || NiFeOx (+), Pt/C (-) || NiFeOx (+), and NiFe PPc (-) || NiFeOx (+) in 1.0 M KOH.

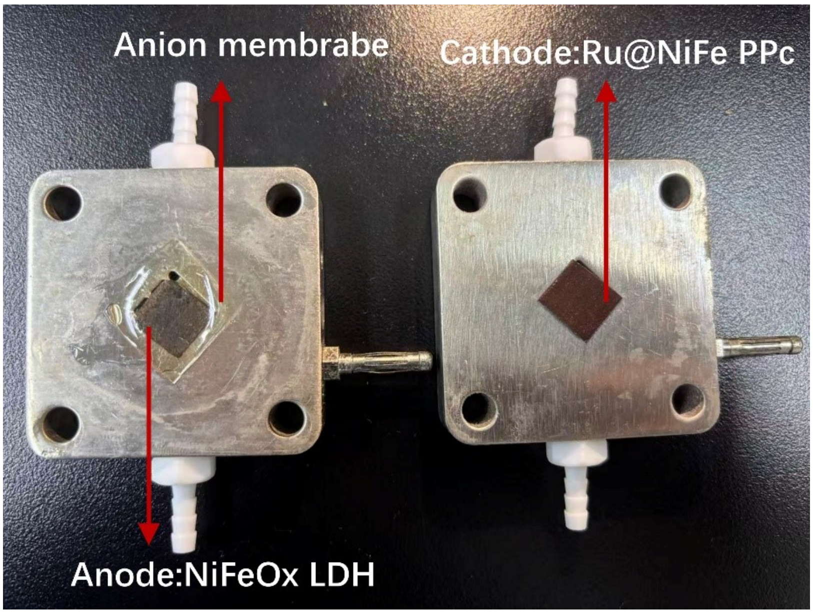

Fig. S33 The diagram of alkaline electrolyzer configuration.

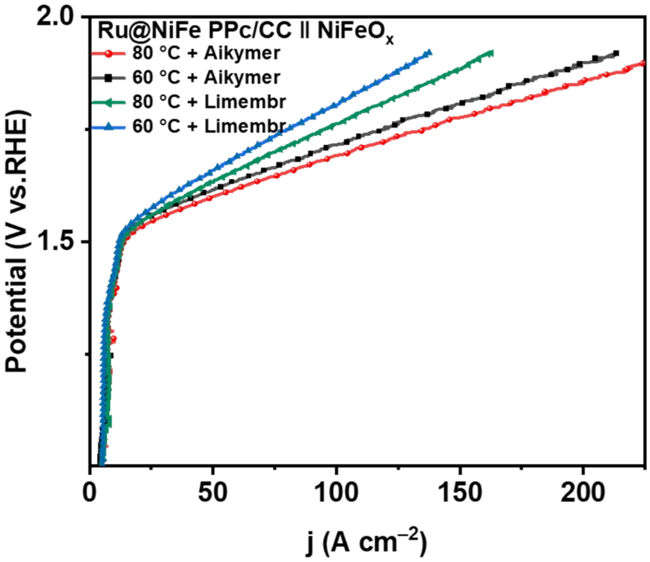

Fig. S34 Performance evaluation of the practical hydrogen evolution capability of Ru@NiFe PPc in a bipolar electrolyzer with an anion exchange membrane at different temperatures in 1 M KOH.

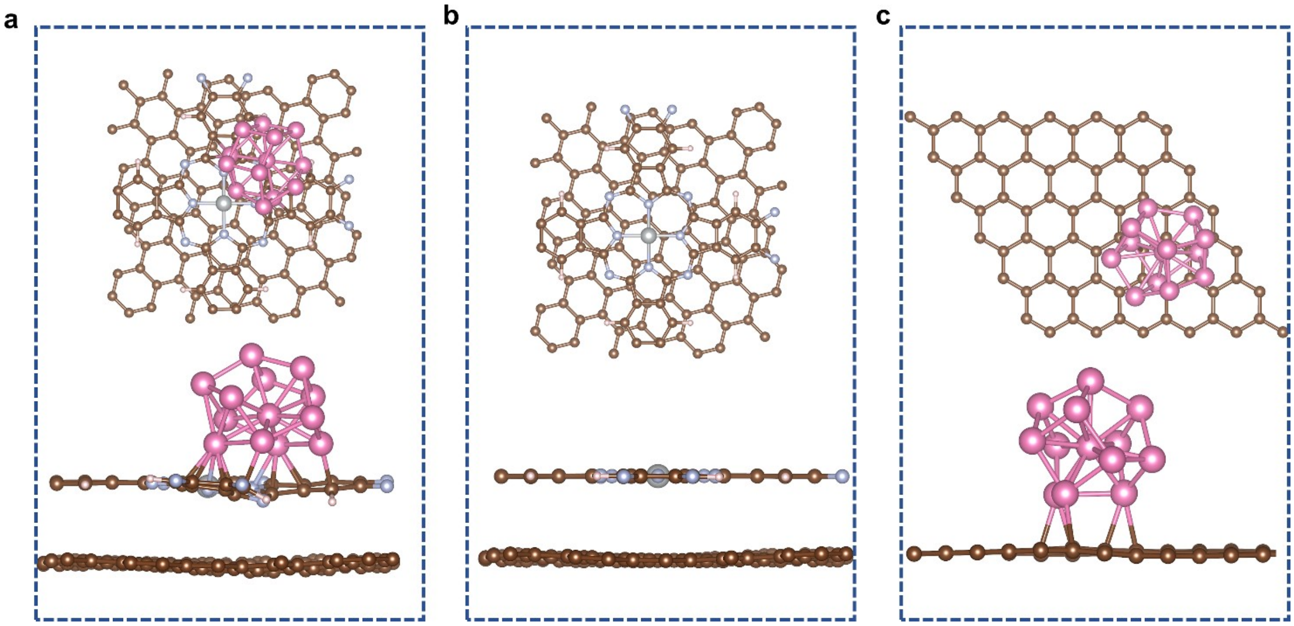

Fig. S35 Theoretical calculation model of (a) Ru@NiFe PPc, (b) NiFe PPc, and (c) Ru@G Ru, pink, N, light blue, and C, grey.

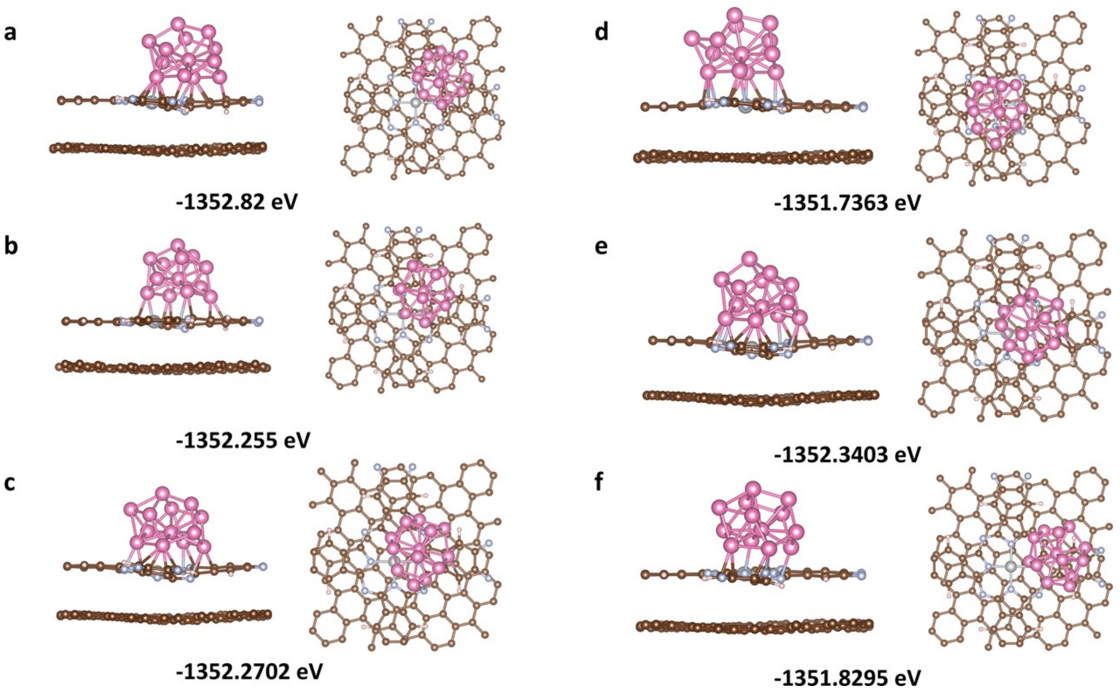

Fig. S36 DFT-calculated optimized structures of Ru–N coordination sites at different locations on the Ru@NiFe PPc. The absolute energies are shown below each configuration.

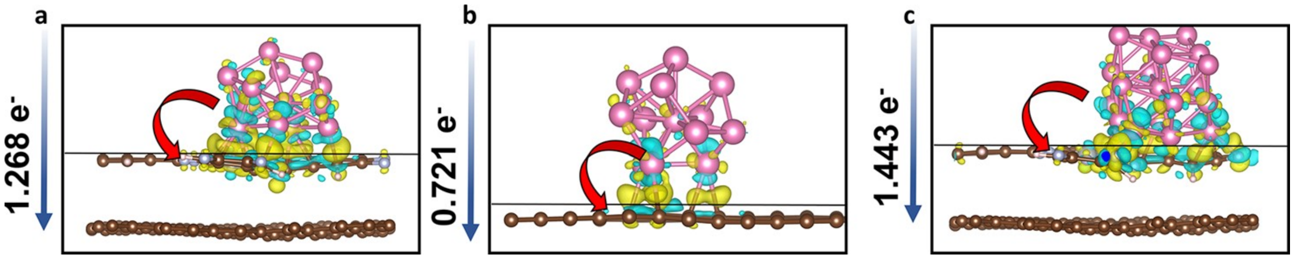

Fig. S37 Charge density difference of (Δ*ρ*). (a) Ru@NiFe PPc, (b) Ru@G, (c) Ru19@NiFe PPc.

Note: Charge-density difference analysis reveals pronounced electron accumulation at the Ru–N interfaces, indicating strong electronic coupling between the Ru nanoparticles and the NiFe PPc framework. The charge-density difference (Δρ) calculations show that, in the Ru@NiFe PPc model, the Ru nanoparticles donate 1.268 e^- to the 2D NiFe PPc/graphene heterostructure, whereas in the Ru@G model transfer only 0.721 e^- and Ru19@NiFe PPc model transfer 1.443 e^- to 2D NiFe PPc/graphene heterostructure .

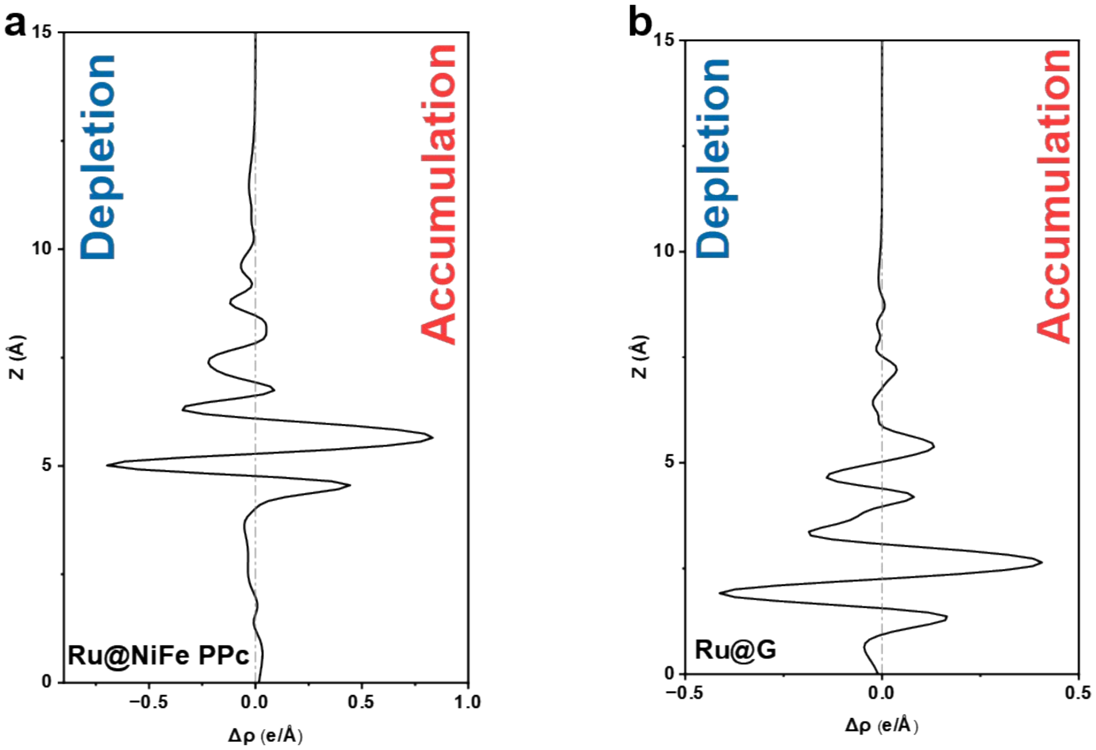

Fig. S38 Averaged charge density difference ($\Delta\rho$): (a) Ru@NiFe PPc, (b) Ru@G.

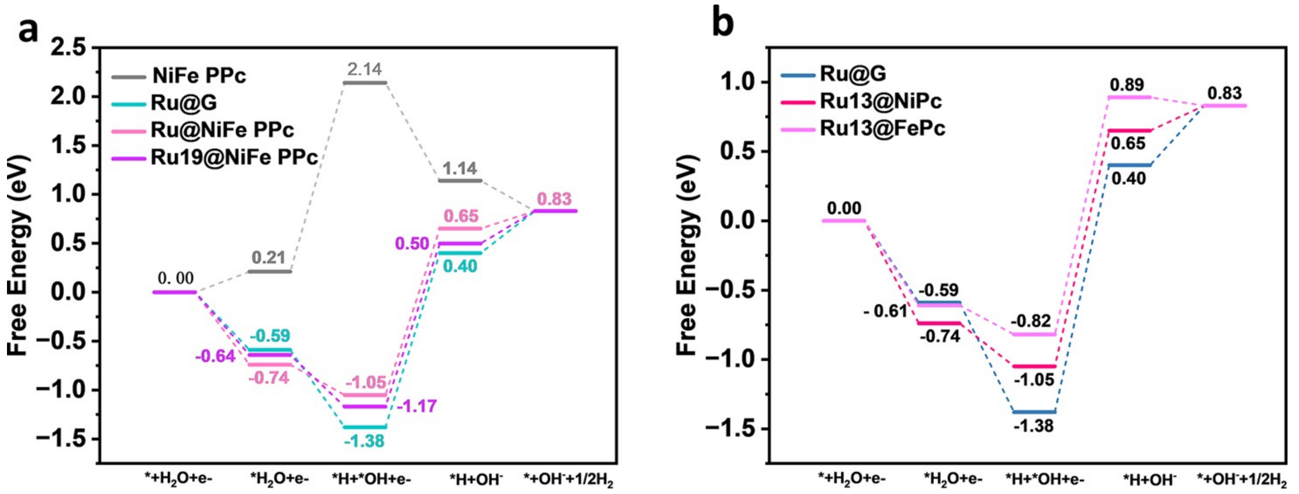

Fig. S39 (a) Calculated free energy diagram for hydrogen migration path on Ru@NiFe PPc, Ru@G, NiFe PPc and Ru19@NiFe PPc. (b)Calculated free energy diagram for hydrogen migration path on Ru@G, Ru13@NiPc and Ru13@FePc.

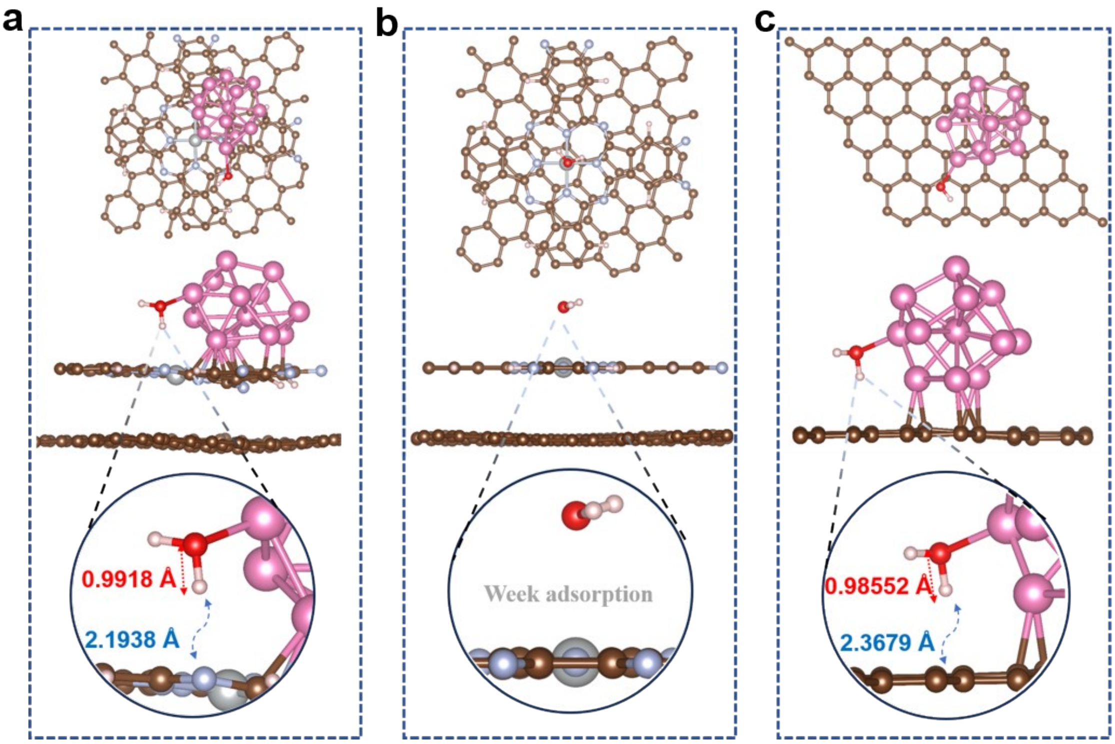

Fig. S40 Theoretical calculation model of dsorption models of water on different materials. (a) Ru@NiFe PPc, (b) NiFe PPc, and (c) Ru@G. Ru, pink, N, light blue, O, red, H, white and C, grey.

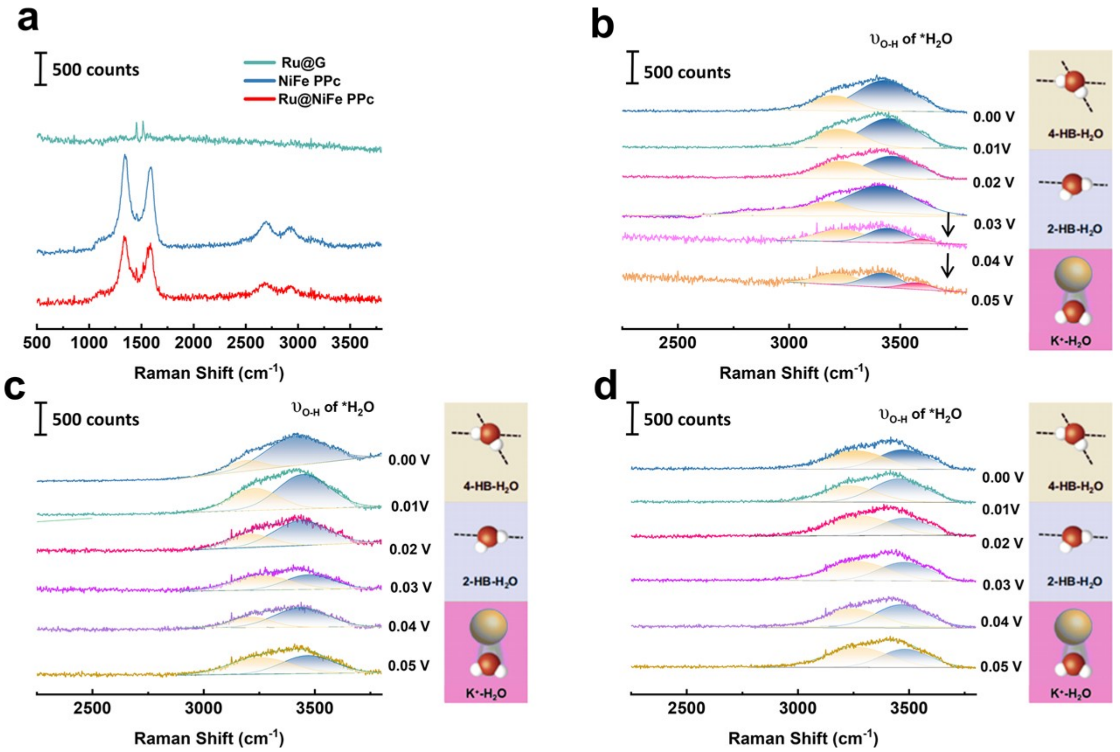

Fig. S41 (a) Raman spectra of Ru@NiFe PPc, NiFe PPc and Ru@G. In situ Raman spectra during the alkaline HER in 1 M KOH after holding the potential (b) Ru@NiFe PPc, (c) NiFe PPc and (d) Ru@G.

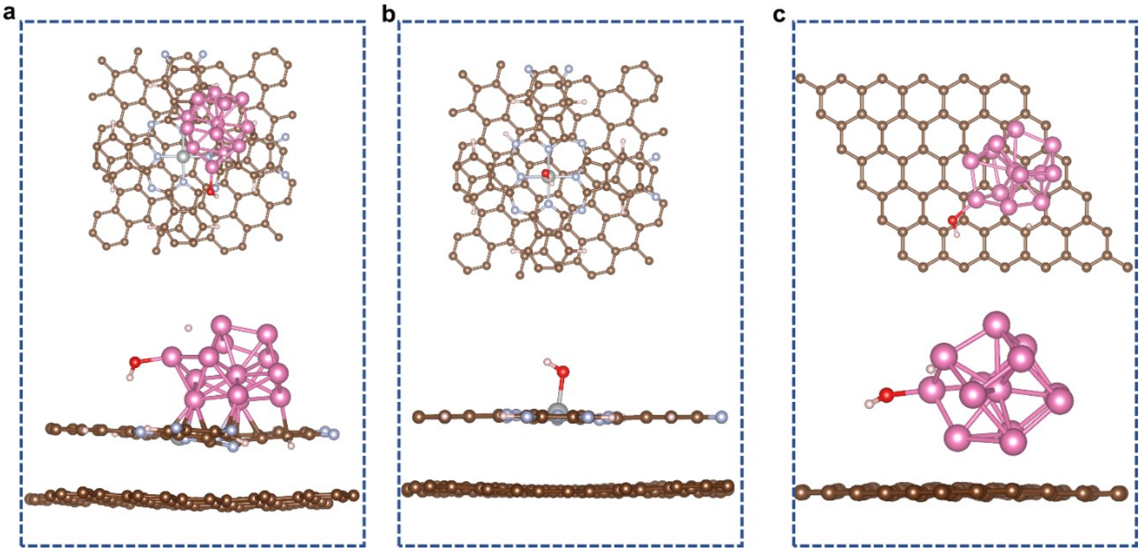

Fig. S42 Theoretical calculation model of desorption models of *OH on different materials. (a) Ru@NiFe PPc, (b) NiFe PPc, and (c) Ru@G. Ru, pink, N, light blue, O, red, H, white and C, grey.

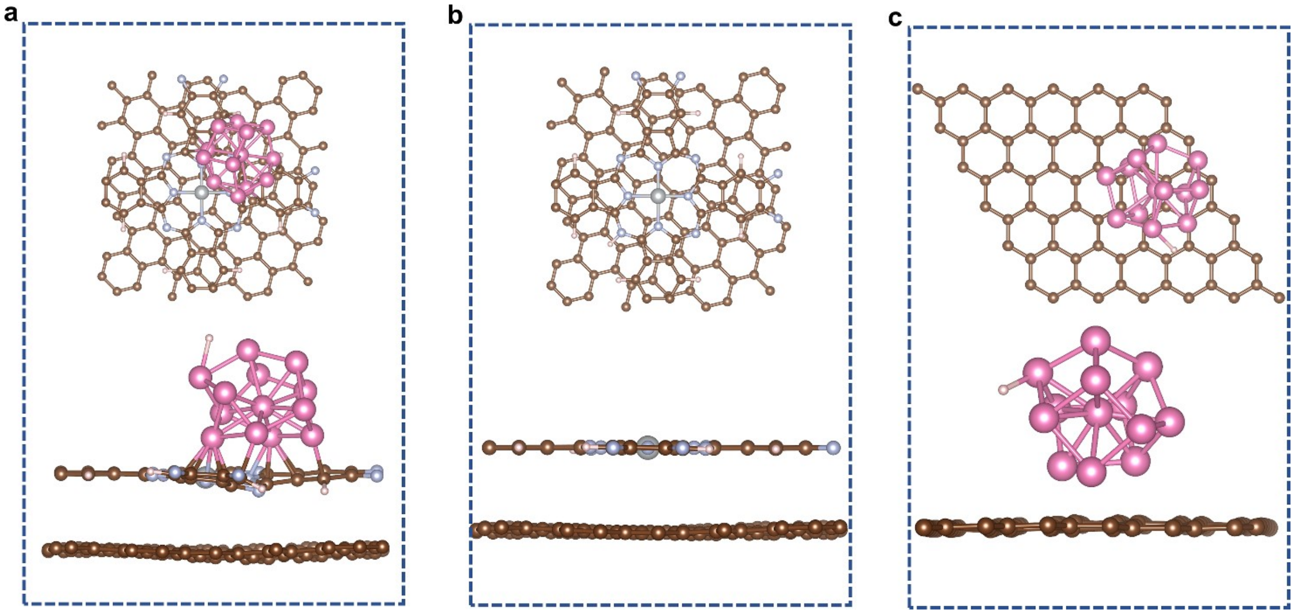

Fig. S43 Theoretical calculation model of desorption models of *H on different materials. (a) Ru@NiFe PPc, (b) NiFe PPc, and (c) Ru@G. Ru, pink, N, light blue, H, white and C, grey.

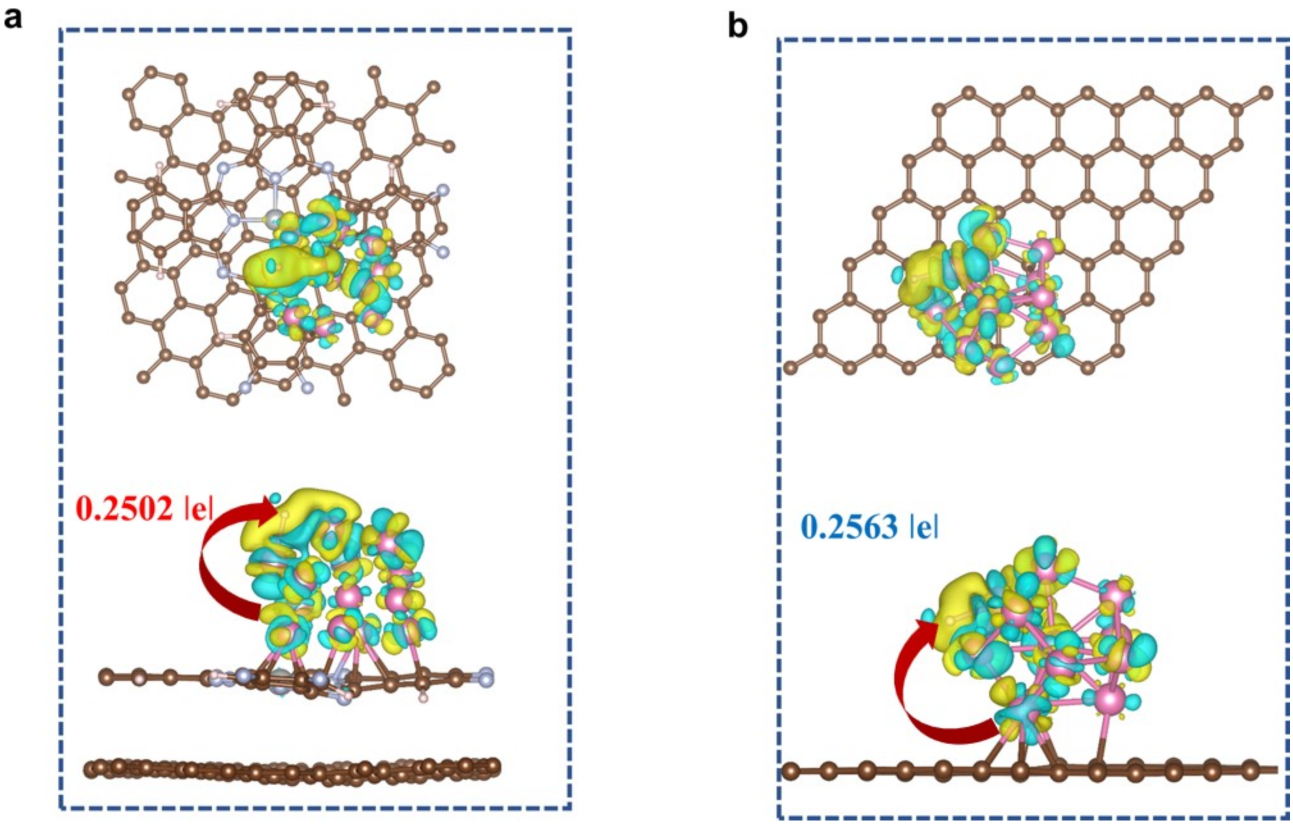

Fig. S44 Theoretical calculation model of desorption models and Bader charge analysis of *H adsorbed on (a) Ru@NiFe PPc and (b) Ru@G. Blue and yellow represent electron depletion and accumulation, respectively isosurface set to 0.001.

Note: Bader charge analysis reveals that the amount of charge transferred from Ru to *H is 0.2563 |e| for the Ru@G model and 0.2502 |e| for the Ru@NiFe PPc model. The slightly lower charge transfer in the latter indicates a weakened *H adsorption strength on Ru@NiFe PPc. This reduction in electron donation suggests that the NiFe coordination environment subtly modulates the electronic structure of the Ru active site, thereby altering the Ru–H interaction. Such electronic tuning may have important implications for the hydrogen adsorption–desorption equilibrium and ultimately for the catalytic performance of the Ru@NiFe PPc system.

Table S1. Elemental contents of C, N, O, Fe, Ni and Ru based on SEM analysis for FeTNPc, NiTNPc and NiTAPc.

Samples	Chemical composition (at %)				
	C	N	O	Ni	Fe
FeTNPc	88.84	5.90	4.56	-	0.70
NiTNPc	88.44	8.26	2.64	0.66	-
NiTAPc	81.73	11.3	6.11	0.86	-

Table S2. Elemental contents of C, N, O, Fe, Ni and Ru based on TEM analysis for NiFe PPc and Ru@NiFe PPc.

Samples	Chemical composition (at %)					
	C	N	O	Ni	Fe	Ru
NiFe PPc	87.91	1.91	2.20	4.09	3.03	-
Ru@NiFe PPc	97.14	0.94	1.50	0.26	0.08	0.08

Table S3. Elemental contents of C, N, O, Fe, Ni and Ru based on XPS analysis for NiFe PPc and Ru@NiFe PPc.

Samples	Chemical composition (at %)					
	C	N	O	Ni	Fe	Ru
NiFe PPc	71.11	17.64	9.07	1.21	0.96	-
Ru@NiFe PPc	57.54	4.21	19.02	0.19	0.60	18.42

Table S4. ICP-OES results of the Ru@NiFe PPc and NiFe PPc cathodes.

Samples	Elemental composition (wt%)		
	Ni	Fe	Ru
Ru@NiFe PPc	0.0491	0.0149	0.2729
NiFe PPc	0.04524	0.01489	-

Table S5. EXAFS fitting parameters for Ru@NiFe PPc.

Samples	Bond type	Coordination number	Bond length (Å)	Debye-Waller factor σ^2 (10^{-2} Å^2)	R factor
Ru@NiFe PPc	Ru-Ru	5.9	2.66	1.4	0.007
	Ru-N	2.0	2.01	0.3	

Note: S_0^2 was fixed to 0.98 as firstly determined from Ru foil fitting. The fitting range for Ru@NiFe PPc is: $3.6 \leq k$ (Å^{-1}) ≤ 11.4; $1.1 \leq R$ (Å) ≤ 3.

Table S6. Comparison of C_{dl}, ECSA, and Contact angle of Ru@NiFe PPc, NiFe PPc, and Pt/C catalysts during HER process under 1.0 M KOH solution.

Catalysts	C_{dl} (mF cm^{-2})	ECSA (m^{2}g^{-1} pt)	Contact angle (°)
Ru@NiFe PPc	18.64	466	12.3
NiFe PPc	46.06	401.5	141.0
Pt/C	4.40	110	143.7
Ru@G	16.17	404.25	58.1

Table S7. Rs, Rct values corresponding to EIS Nyquist fitting circuit diagram of Ru@NiFe PPc, NiFe PPc, and Pt/C catalysts during HER process under 1.0 M KOH solution.

Samples	Rs (Ω)	R1 (Ω)
Ru@NiFe PPc	0.684	1.861
NiFe PPc	0.500	3.732
Pt/C	0.388	1.843

Table S8. ICP-OES results of the Ru@NiFe PPc and Ru@NiFe PPc before and after 3000 cv cycles cathodes.

Samples	Elemental composition (wt%)		
	Ni	Fe	Ru
Ru@NiFe PPc	0.0491	0.0149	0.2729
Ru@NiFe PPc after 3000 cv cycles	0.0413	0.0222	0.2150

Table S9. ICP-OES results of the electrolyte collected before and after 3000 CV cycles using Ru@NiFe PPc cathodes.

Samples	Elemental composition (wt%)		
	Ni	Fe	Ru
electrolyte	0.000301	0.000398	0.000192
electrolyte after 3000 cv cycles	0.000181	0.000347	0.000131

Table S10. Comparison of the HER performance of Ru@NiFe PPc with reported catalysts in alkaline conditions.

Catalysts	η@10mA/cm^2 (mV)	Tafel slope (mV/dec)	Reference
Ru@NiFe PPc	15	34	This Work
NiFelr-LDH	51	56	*Appl. Catal. B-Environ.* **2021**, 284, 119740[5]
Ru-NiFeP	44	80	*Applied Surface Science* **2021**, 536, 147952[6]
RuCoP/CDs	51	73.4	*Angew. Chem. Int. Ed.* **2021**, 60, 7234[7]
h-$RuSe_2$	34	63	*Angew. Chem. Int. Ed.* 133, 7089-7093 **(2021)**[8]
N-Co_2P	34	41	*ACS Catal.* 9, 3744- 3752 **(2019)**[9]
Ru-MoS/CC	41	114	*Appl. Catal. B-Environ.* **2019**, 249, 91[10]
Ru-NiCoP/NF	44	45.4	*Appl. Catal. B-Environ.* **2020**.279, 119396[11]
RhSez	81.6	80	*Adv. Mater.* 33, 2007894 **(2021)**[12]
Ni-MOF@Pt	102	88	*Nano. Lett.* **2019**, 19, 8447[13]
Fe-NiPv	80	48	*Adv. Mater.* **2024**, 36, 2307395[14]
Ni/NC	130	82	*Nanoscale*, 14, **(2022)**, 6202-6211[15]
N-Ni-S	134	113	*Appl. Catal. B: Environ.* 276 **(2020)**
$NiSe_2$@NC-PZ	162	88	*Appl. Catal. B: Environ.* 272 **(2020)**[16]
C@NiNPs	174	153.84	*Appl. Catal. B: Environ.* 321 **(2023)**[17]
Ni_3FeN@NC	181	119	*Carbon* 163 **(2020)** 178-185[18]
$NiSe_2$@NC-DO	208	150	*Appl. Catal. B: Environ.* 272 **(2020)**[16]

Table S11. Performance comparison of our AEMWEs with other AEMWEs reported in previous literatures.

Catalysts (cathode || anode)	Current density (A/cm^2)	Reference
Ru@NiFe PPc || NiFeOx LDH	**2.00 at 2.09 Vcell**	**This work**
Pt/C || NiFe-LDH	1.00 at 2.03 V_{cell}	*Energy Environ. Sci.*, **2024**, 17, 1397-1406[19]
Ru1-Mo2C || NiFe-LDH	2.00 at 2.03 Vcell	*Energy Environ. Sci.*, **2024**, 17, 1397-1406[19]
Ru/NDC-4 || IrO_2	0.72 at 2.00 Vcell	*Appl. Catal. B*, **2023**, 327, 122466[20]
Ru-Ru_2P/V_2CT_x || RuO_2	2.00 at 2.04 Vcell	*Appl. Catal. B*, **2024**, 343, 123517[21]
α-$Co(OH)_2$@Ru || RuO_2	0.52 at 2.00 Vcell	*Small Methods*, **2023**, 7, 2201362[22]
Pt mesh || S-FeOOH	1.00 at 1.99 Vcell	*Appl. Catal. B*, **2022**, 315, 121571[23]
PtRu/C || IrO_2	1.15 at 2.00 Vcell	*Nature Energy*, **2020**, 5, 378-385[24]
Ir@Zr-CoP || Ir@Zr-CoP	2.00 at 2.13 Vcell	*Adv. Energy Mater.*, **2023**, 13, 2301841[25]
Pt/C || IrO_2	1.00 at 2.04 Vcell	*J. Ind. Eng. Chem.* **2019**, 76, 410-418[26]
NiMoCo || NiMoCo	1.00 at 2.11 Vcell	*Small*, **2022**, 18, 2200303[27]
MoO2/MoNi4 || HS-RuCo/NC	1.00 at 2.07 Vcell	*Small*, **2023**, 19, 2207611[28]
NA-LT-CA || NA-LT-CA	0.80 at 1.98 Vcell	*Chem. Eng. J.*, **2024**, 486, 150180[29]
NA-CA || NA-CA	0.50 at 2.05 Vcell	*Chem. Eng. J.*, **2024**, 486, 150180[29]

Reference

1. G. Henkelman, A. Arnaldsson and H. Jónsson, *Comput. Mater. Sci.*, 2006, **36**, 354-360.
2. J. P. Perdew and Y. Wang, *Phys. Rev. B*, 1992, **45**, 13244-13249.
3. S. Grimme, *J. Comput. Chem.*, 2006, **27**, 1787-1799.
4. E. Sanville, S. D. Kenny, R. Smith and G. Henkelman, *J. Comput. Chem.*, 2007, **28**, 899-908.
5. H. Sun, W. Zhang, J.-G. Li, Z. Li, X. Ao, K.-H. Xue, K. K. Ostrikov, J. Tang and C. Wang, *Appl. Catal. B Environ.*, 2021, **284**, 119740.
6. Y. Lin, M. Zhang, L. Zhao, L. Wang, D. Cao and Y. Gong, *Appl. Surf. Sci.*, 2021, **536**, 147952.
7. H. Song, M. Wu, Z. Tang, J. S. Tse, B. Yang and S. Lu, *Angew. Chem. Int. Ed.*, 2021, **60**, 7234-7244.
8. Y. Zhao, H. Cong, P. Li, D. Wu, S. Chen and W. Luo, *Angew. Chem. Int. Ed.*, 2021, **60**, 7013-7017.
9. Y. Men, P. Li, J. Zhou, G. Cheng, S. Chen and W. Luo, *ACS Catal.*, 2019, **9**, 3744-3752.
10. D. Wang, Q. Li, C. Han, Z. Xing and X. Yang, *Appl. Catal. B Environ.*, 2019, **249**, 91-97.
11. D. Chen, R. Lu, Z. Pu, J. Zhu, H.-W. Li, F. Liu, S. Hu, X. Luo, J. Wu, Y. Zhao and S. Mu, *Appl. Catal. B Environ.*, 2020, **279**, 119396.
12. W. Zhong, B. Xiao, Z. Lin, Z. Wang, L. Huang, S. Shen, Q. Zhang and L. Gu, *Adv. Mater.*, 2021, **33**, e2007894.
13. K. Rui, G. Zhao, M. Lao, P. Cui, X. Zheng, X. Zheng, J. Zhu, W. Huang, S. X. Dou and W. Sun, *Nano Lett.*, 2019, **19**, 8447-8453.
14. X. Liu, Q. Yu, X. Qu, X. Wang, J. Chi and L. Wang, *Adv. Mater.*, 2024, **36**, e2307395.
15. L. Hu, J. Shi, Z. Peng, Z. Zheng, H. Dong and T. Wang, *Nanoscale*, 2022, **14**, 6202-6211.
16. H. Chen, F. Goodarzi, Y. Mu, S. Chansai, J. J. Mielby, B. Mao, T. Sooknoi, C. Hardacre, S. Kegnæs and X. Fan, *Appl. Catal. B Environ.*, 2020, **272**, 119013.
17. A. Arandia, J. Yim, H. Warraich, E. Leppäkangas, R. Bes, A. Lempelto, L. Gell, H. Jiang, K. Meinander, T. Viinikainen, S. Huotari, K. Honkala and R. L. Puurunen, *Appl. Catal. B Environ.*, 2023, **321**, 122046.
18. N. Cheng, N. Wang, L. Ren, G. Casillas-Garcia, N. Liu, Y. Liu, X. Xu, W. Hao, S. X. Dou and Y. Du, *Carbon*, 2020, **163**, 178-185.
19. T. Chao, W. Xie, Y. Hu, G. Yu, T. Zhao, C. Chen, Z. Zhang, X. Hong, H. Jin, D. Wang, W.

Chen, X. Li, P. Hu and Y. Li, *Energy Environ. Sci.*, 2024, **17**, 1397-1406.

20. J.-T. Ren, L. Chen, H.-Y. Wang, W.-W. Tian, X. Zhang, T.-Y. Ma, Z. Zhou and Z.-Y. Yuan, *Appl. Catal. B Environ.*, 2023, **327**, 122466.
21. T. H. Nguyen, P. K. L. Tran, D. T. Tran, V. A. Dinh, N. H. Kim and J. H. Lee, *Appl. Catal. B Environ.*, 2024, **343**, 123517.
22. J. Zhao, J. Wang, X. Zheng, H. Wang, J. Zhang, J. Ding, X. Han, Y. Deng and W. Hu, *Small Methods*, 2023, **7**, 2201362.
23. X.-Y. Zhang, F.-T. Li, Y.-W. Dong, B. Dong, F.-N. Dai, C.-G. Liu and Y.-M. Chai, *Appl. Catal. B Environ.*, 2022, **315**, 121571.
24. D. Li, E. J. Park, W. Zhu, Q. Shi, Y. Zhou, H. Tian, Y. Lin, A. Serov, B. Zulevi, E. D. Baca, C. Fujimoto, H. T. Chung and Y. S. Kim, *Nat. Energy*, 2020, **5**, 378-385.
25. Q. P. Ngo, T. T. Nguyen, Q. T. T. Le, J. H. Lee and N. H. Kim, *Adv. Energy Mater.*, 2023, **13**, 2301841.
26. A. Lim, H.-j. Kim, D. Henkensmeier, S. Jong Yoo, J. Young Kim, S. Young Lee, Y.-E. Sung, J. H. Jang and H. S. Park, *J. Ind. Eng. Chem.*, 2019, **76**, 410-418.
27. M. H. Wang, Z. X. Lou, X. Wu, Y. Liu, J. Y. Zhao, K. Z. Sun, W. X. Li, J. Chen, H. Y. Yuan, M. Zhu, S. Dai, P. F. Liu and H. G. Yang, *Small*, 2022, **18**, 2200303.
28. J. Du, D. Chen, Y. Ding, L. Wang, F. Li and L. Sun, *Small*, 2023, **19**, 2207611.
29. X. Jiang, V. Kyriakou, B. Wang, S. Deng, S. Costil, C. Chen, T. Liu, C. Deng, H. Liao and T. Jiang, *Chem. Eng. J.*, 2024, **486**, 150180.